AN IMMERSED DISCONTINUOUS GALERKIN METHOD FOR ACOUSTIC WAVE PROPAGATION IN INHOMOGENEOUS MEDIA[*]

SLIMANE ADJERID[†] AND KIHYO MOON[‡]

Abstract. We present an immersed discontinuous Galerkin finite element method on Cartesian meshes for two dimensional acoustic wave propagation problems in inhomogeneous media where elements are allowed to be cut by the material interface. The proposed method uses a discontinuous Galerkin finite element formulation with polynomial approximation on elements that contain one fluid, while on interface elements containing more than one fluid it uses specially built piecewise polynomial shape functions that satisfy appropriate interface jump conditions. The finite element spaces on interface elements satisfy physical interface conditions from the acoustic problem as well as additional interface conditions derived from the system of partial differential equations. We present several computational results that show that the proposed method has desirable stability properties and optimal convergence rates. Several computational examples are included with linear and curved interfaces.

Key words. wave propagation, immersed finite element, discontinuous Galerkin, acoustics

AMS subject classifications. 65M20, 65M60

DOI. 10.1137/16M1090934

1. Introduction. Wave propagation in inhomogeneous media is ubiquitous in nature, appearing in acoustics, elasticity, and electromagnetism. Wave propagation in inhomogeneous media is modeled by hyperbolic partial differential equations with discontinuous coefficients which reflect the fact that waves travel at different speeds in different media. Appropriate interface conditions are added to the pertinent partial differential equations to obtain a unique solution.

The discontinuous Galerkin (DG) method has the following main advantages over the traditional finite difference and finite volume methods: (i) it can use arbitrarily high degree polynomials, (ii) it can handle complex geometries with simple treatment of boundary conditions, (iii) it is highly parallelizable, and (iv) it simplifies local p-refinement (degree variation) and h-refinement (mesh size variation). The DG method was introduced in the early seventies to solve neutron transport problems [33] and mainly lay dormant for approximately fifteen years before the work of Cockburn and Shu [14] and Cockburn, Lin, and Shu [13] on Runge–Kutta DG methods for nonlinear hyperbolic conservation laws [13, 14] launched new interest. The DG method is now well established and for more on its history, properties, and applications the reader may consult the books [15, 21, 32, 34]. Two popular DG formulations have been used to solve transient linear hyperbolic systems: (i) semidiscrete DG methods using a method-of-lines approach [20] where the problem is first discretized in space using a DG formulation combined with time integrators and (ii) space-time DG methods [16]. Our immersed finite element (IFE) method is a method-of-lines approach.

[†]Department of Mathematics Virginia Tech, Blacksburg, VA 24061-0123 (adjerids@math.vt.edu).

[‡]SAMSUNG, Seoul, South Korea (hyoxt121@gmail.com).

Conventional finite element methods on body-fitted meshes [8] can be applied to solve interface problems. However, the restriction that no element is allowed to be cut by the interface leads to several drawbacks, such as (i) the need for a large number of remeshing steps when solving problems with moving interfaces, (ii) excessive mesh refinement to resolve small structures such as thin layers in the domain, and (iii) prohibition of the use of uniform meshes when solving general interface problems. In order to circumvent these limitations, optimal linear IFE methods allowing finite elements to be cut by the interface were proposed [5, 18, 22, 26]. The IFE methods use meshes that are not necessarily body fitted with specially designed piecewise polynomial finite element spaces satisfying interface jump conditions. Elements that are cut by the interface are referred to as interface elements; otherwise, they are called noninterface elements. In general, problems are solved on meshes containing both interface and noninterface elements.

Nonpolynomial spaces were constructed by solving local problems and were used in the generalized finite element method (GFEM) [8]. Later, Belytschko et al. developed the extended finite element method (X-FEM) [10]. The IFE, GFEM, and X-FEM methods share the same goal of constructing special finite element spaces to resolve local features of the solution. The IFE approach relies purely on piecewise polynomials in each element while GFEM and X-FEM may use nonpolynomial spaces. Optimal IFE methods have been developed for diffusive [2, 6, 17, 22], elasticity [28], and Stokes [4] problems. Several interface problems have been also solved by immersed finite difference methods [27, 29] on nonfitted grids.

In this manuscript we present a discontinuous finite method for solving acoustic wave propagation problems in inhomogeneous media on a square domain with nonfitted square meshes. We follow the work of Adjerid and Moon [7] and Moon [30] for the one dimensional acoustic interface problem to construct second and third order DG methods for the two dimensional acoustic interface problem. The main contributions of this work can be summarized as (i) a weighted weak immersed DG method referred to as IDG when exact integration is used or IDG-NI when numerical integration is used and (ii) a procedure to construct piecewise bilinear and biquadratic IFE spaces. The IFE spaces are constructed with respect to linear and curved interfaces for the two dimensional acoustic interface problem on square meshes. Numerical computations show that the IFE spaces exhibit optimal approximation capabilities for discontinuous solutions across the interface with moderate and high contrasts. Furthermore, they suggest that the proposed methods are stable for all contrasts on a fixed mesh and fixed interface.

This paper is organized as follows: we state the interface acoustic problem in section 2 and in section 3 we describe an algorithm to construct IFE basis functions and spaces on interface elements. In section 4 we derive our IDG formulation for the acoustic interface problem and prove that it is stable. In section 5 we present numerical results for several wave propagation examples with linear and curved interfaces to show the optimality of the IFE spaces and stability of the IDG method. We conclude with a few remarks in section 6.

2. Problem statement. Let $\mathbf{v} = [u, v]^t$ and p, respectively, be the velocity vector and pressure defined on a two dimensional domain Ω consisting of two open subdomains Ω_1 and Ω_2 separated by an interface Γ such that $\Omega = \Omega_1 \cup \Omega_2 \cup \Gamma$ and $\tilde{\Omega} = \Omega_1 \cup \Omega_2$ and with $\partial\Omega$ denoting the boundary of Ω as illustrated in Figure 1. We assume that $\mathbf{v}$ and p satisfy the acoustic problem
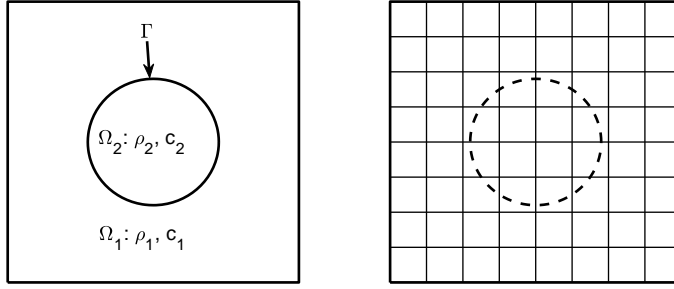
FIG. 1. *A domain containing two fluids separated by an interface Γ (left) and a nonfitting mesh (right).*

(1a)
$$\begin{cases} \dfrac{\partial p}{\partial t} + \rho c^2 \nabla \cdot \mathbf{v} = 0, \\[2mm] \dfrac{\partial \mathbf{v}}{\partial t} + \dfrac{1}{\rho}\nabla p = 0, \end{cases} \quad (x,y) \in \tilde{\Omega} \quad t > 0,$$

where the density ρ and the speed of sound c are piecewise constant functions such that $c|_{\Omega_i} = c_i$ and $\rho|_{\Omega_i} = \rho_i$, $i = 1, 2$, as illustrated in Figure 1.

Letting $\boldsymbol{\nu} = (\nu_x, \nu_y)^t$ denote the unit normal vector on the interface Γ pointing towards Ω_1, the pressure and velocity satisfy the interface conditions

(1b)
$$[p]_\Gamma = 0, \qquad [\mathbf{v} \cdot \boldsymbol{\nu}]_\Gamma = 0,$$

where at $(x,y) \in \Gamma$, $[w] = \lim_{\tau \to 0} w_1((x,y) - \tau\boldsymbol{\nu}) - \lim_{\tau \to 0} w_2((x,y) + \tau\boldsymbol{\nu})$ denotes the jump across the interface with $w|_{\Omega_l} = w_l$, $l = 1, 2$. This system has a unique solution given initial and appropriate boundary conditions.

Next, we write the acoustic problem as a first order symmetrizable linear hyperbolic system of partial differential equations for $\mathbf{U} = [p, u, v]^t$ having the form

(2a)
$$\frac{\partial \mathbf{U}}{\partial t} + \mathbf{A}\frac{\partial \mathbf{U}}{\partial x} + \mathbf{B}\frac{\partial \mathbf{U}}{\partial y} = 0, \ (x,y) \in \tilde{\Omega}, \ t > 0,$$

where

(2b) $\quad \mathbf{A}|_{\Omega_i} = \mathbf{A}_i = \begin{pmatrix} 0 & \rho_i c_i^2 & 0 \\ \frac{1}{\rho_i} & 0 & 0 \\ 0 & 0 & 0 \end{pmatrix}, \ \mathbf{B}|_{\Omega_i} = \mathbf{B}_i = \begin{pmatrix} 0 & 0 & \rho_i c_i^2 \\ 0 & 0 & 0 \\ \frac{1}{\rho_i} & 0 & 0 \end{pmatrix}, \ i = 1, 2.$

In order to construct the numerical flux we note that every $n \times n$ symmetrizable matrix can be factored as $\mathbf{A} = \mathbf{P}\boldsymbol{\Lambda}\mathbf{P}^{-1}$, where $\boldsymbol{\Lambda} = diag(\lambda_1, \lambda_2, \ldots, \lambda_n)$, and if $|\boldsymbol{\Lambda}| = diag(|\lambda_1|, |\lambda_2|, \ldots, |\lambda_n|)$ and $\boldsymbol{\Lambda}^\pm = \frac{\boldsymbol{\Lambda} \pm |\boldsymbol{\Lambda}|}{2}$ we define $\mathbf{A}^\pm = \mathbf{P}\boldsymbol{\Lambda}^\pm\mathbf{P}^{-1}$.

If, for instance, the system (2) is subjected to the interface conditions (1b) and the inflow boundary conditions $\mathbf{D}(\mathbf{n})^-\mathbf{U}|_{\partial\Omega} = g$, where $\mathbf{D}(\mathbf{n}) = \mathbf{A}n_x + \mathbf{B}n_y$, $\mathbf{n} = (n_x, n_y)^t$ is the unit outward normal vector on $\partial\Omega$, and the initial condition $\mathbf{U}(x,y,0) = \mathbf{U}_0(x,y)$, then in Ω it admits a unique solution.

In order to apply the DG method to the acoustic problem (2) we partition the domain Ω into $N = n^2$ square elements and use standard polynomials on noninterface elements containing one fluid and specially designed piecewise polynomial IFE shape functions on interface elements containing two fluids. We start by showing how to construct interface polynomial spaces and shape functions.

3. Interface finite element shape functions and spaces. In this section we discuss a procedure to construct IFE approximations and start by deriving interface jump conditions.

3.1. Interface jump conditions. Elements containing one fluid are equipped with standard polynomial shape functions while elements containing two fluids separated by an interface will be equipped with piecewise polynomial functions: one piece on each fluid which are connected together by jump conditions across the interface. Applying the physical interface condition (1b) leads to continuous immersed shape functions for the pressure while only the normal component of immersed shape functions for the velocity is continuous on linear interfaces. To obtain a reduced number of high-degree immersed shape functions we need additional interface conditions which are derived from compatibility conditions obtained from the acoustic problem subjected to smooth initial and boundary conditions. A similar technique was used by Henshaw to derive compatibility conditions for Maxwell's equations [19] and Henshaw et al. for a fluid-structure interface problem [9].

More precisely, alternate partial differential equations for the acoustic problem are obtained by differentiating the first equation in (1a) with respect to t and using the second equation in (1a) to replace $\partial \mathbf{v}/\partial t$ in the right-hand side to show that the pressure satisfies the second order wave equation. Similarly, the velocity also satisfies a second order equation. Thus, we have

$$(3) \qquad \frac{\partial^2 p}{\partial t^2} = c^2 \Delta p, \qquad \frac{\partial^2 \mathbf{v}}{\partial t^2} = c^2 \nabla(\nabla \cdot \mathbf{v}) \qquad \text{on } \tilde{\Omega}.$$

From (3) one can easily show that on $\tilde{\Omega}$ and $t > 0$ we have

$$(4) \qquad \frac{\partial^{2m} p}{\partial t^{2m}} = c^{2m} \Delta^m p, \quad \frac{\partial^{2m} \mathbf{v}}{\partial t^{2m}} = c^{2m}(\nabla\nabla\cdot)^m \mathbf{v}, \; m = 1, 2, \dots.$$

By differentiating (4) with respect to t and applying the acoustic equations (1a) we obtain on $\tilde{\Omega}$ and $t > 0$

$$(5) \qquad \begin{aligned} \frac{\partial^{2m+1} p}{\partial t^{2m+1}} &= c^{2m}\Delta^m \frac{\partial p}{\partial t} &= -c^{2m}\Delta^m(\rho c^2 \nabla \cdot \mathbf{v}), \\ \frac{\partial^{2m+1} \mathbf{v}}{\partial t^{2m+1}} &= c^{2m}(\nabla\nabla\cdot)^m \frac{\partial \mathbf{v}}{\partial t} &= -\frac{c^{2m}}{\rho}\nabla(\Delta^m p), \end{aligned} \qquad m = 1, 2, \dots,$$

which hold for smooth solutions on $\tilde{\Omega}$.

In the remainder of this section we combine the interface jump conditions (1b) with (3), (4), and (5) to derive additional interface jump conditions and construct piecewise polynomial functions satisfying the resulting interface jump conditions.

The physical interface conditions (1b) yield $[\frac{\partial^l p}{\partial t^l}]_\Gamma = 0$ and $[(\frac{\partial^l \mathbf{v}}{\partial t^l}) \cdot \boldsymbol{\nu}]_\Gamma = 0$ for all $l \geq 0$. Thus, we infer from (4) and (5) for $m \geq 0$, that the pressure satisfies

$$(6a) \qquad \left[c^{2m}\Delta^m p \right]_\Gamma = 0,$$

$$(6b) \qquad \left[\frac{c^{2m}}{\rho} \left(\nabla(\Delta^m p) \right) \cdot \boldsymbol{\nu} \right]_\Gamma = 0,$$

while the velocity satisfies

$$(7a) \qquad \left[c^{2m}(\nabla\nabla\cdot)^m \mathbf{v} \right) \cdot \boldsymbol{\nu} \right]_\Gamma = 0,$$

$$(7b) \qquad \left[\rho c^{2m+2}\Delta^m (\nabla \cdot \mathbf{v}) \right]_\Gamma = 0.$$

Applying the relation $(\nabla\nabla\cdot)^m\mathbf{v} = \nabla\Delta^{m-1}(\nabla\cdot\mathbf{v})$ for $m \geq 1$, the jump condition (7a) for $m \geq 1$ may be written as $[c^{2m}(\nabla(\nabla\cdot\Delta^{m-1}\mathbf{v}))\cdot\boldsymbol{\nu}]_\Gamma = 0$.

For instance, for the bilinear IFE shape functions we use the interface conditions (6) and (7) for $m = 0$ to write for the pressure and velocity

$$(8) \qquad [p]_\Gamma = 0, \qquad \left[\frac{1}{\rho}(\nabla p \cdot \boldsymbol{\nu})\right]_\Gamma = 0,$$

$$(9) \qquad [\mathbf{v}\cdot\boldsymbol{\nu}]_\Gamma = 0, \ [\rho c^2(\nabla\cdot\mathbf{v})]_\Gamma = 0.$$

The biquadratic IFE functions for the pressure must satisfy (8) and

$$(10) \qquad [c^2\Delta p]_\Gamma = 0,$$

while the biquadratic velocity must satisfy (9) and

$$(11) \qquad [\mathbf{c}^2(\nabla\nabla\cdot\mathbf{v})\cdot\boldsymbol{\nu}]_\Gamma = 0.$$

Letting Q_k denote the space of polynomial of degree at most $k = 1, 2$ with respect to each variable, we find bilinear Q_1 IFE spaces for the pressure by enforcing (8). The biquadratic Q_2 IFE spaces for the pressure must satisfy (8) and (10). Similarly, we construct bilinear IFE spaces for the velocity by enforcing (9). Finally, the biquadratic IFE spaces for the velocity must satisfy (9) and (11).

3.2. IFE shape functions and spaces. We now turn to the construction of bilinear and biquadratic IFE shape functions and spaces on a square domain and square meshes. First we consider piecewise Q_k, $k = 1, 2$, IFE shape functions on an interface element and assume that the pressure is a piecewise polynomial in Q_k, $k = 1, 2$, while $\mathbf{v}$ is a piecewise polynomial in $(Q_k)^2$, $k = 1, 2$. We further require each of the piecewise polynomial pressure and velocity to satisfy the interface jump conditions discussed in the previous section.

To be more precise let us partition the domain into a uniform square mesh with noninterface elements containing only one fluid and interface elements which are cut by the interface and contain two fluids. Each interface square element $T = \square A_1A_2A_3A_4$ with vertices $A_i = (x_i, y_i)^t$, $i = 1, 2, 3, 4$, is such that the interface Γ intersects two edges at $D = (x_D, y_D)^t$ and $E = (x_E, y_E)^t$ called interface points. The interface $\widetilde{DE} = \Gamma \cap T$ is approximated by the line segment $\overline{DE}$ (for bilinear approximation) to separate T into two polygonal domains T_1 and T_2 such that T_i contains vertices of T that are in Ω_i, $i = 1, 2$. For biquadratic approximation we use $\widetilde{DE}$ to split T into T_1 and T_2. Topologically, we consider reference interface elements of type I with two adjacent edges cut by the interface, type II interface element with two opposite edges cut by the interface, type III element where the interface passes through one vertex and cuts an opposite edge, and type IV where the interface passes through two opposite vertices. All four types of elements are illustrated in Figure 2. The nodes of an interface element are divided into three sets: $\mathcal{I}_0$ denotes the set of nodes on the interface Γ while $\mathcal{I}_j$ denotes the set of nodes of T in Ω_j for $j = 1, 2$.

Let $\mathcal{T}_h$, $\mathcal{T}_h^S$, and $\mathcal{T}_h^I$, respectively, denote the set of all elements in the mesh, the set of all noninterface elements, and the set of all interface elements.

As in standard finite element analysis and computations, the finite element shape functions are constructed on the reference element $\hat{T} = \square \hat{A}_1\hat{A}_2\hat{A}_3\hat{A}_4$ with vertices $\hat{A}_1 = (0, 0)^t$, $\hat{A}_2 = (1, 0)^t$, $\hat{A}_3 = (0, 1)^t$, $\hat{A}_4 = (1, 1)^t$. Let $X = (x, y)^t$ and $\hat{X} = (\hat{x}, \hat{y})^t$ and let

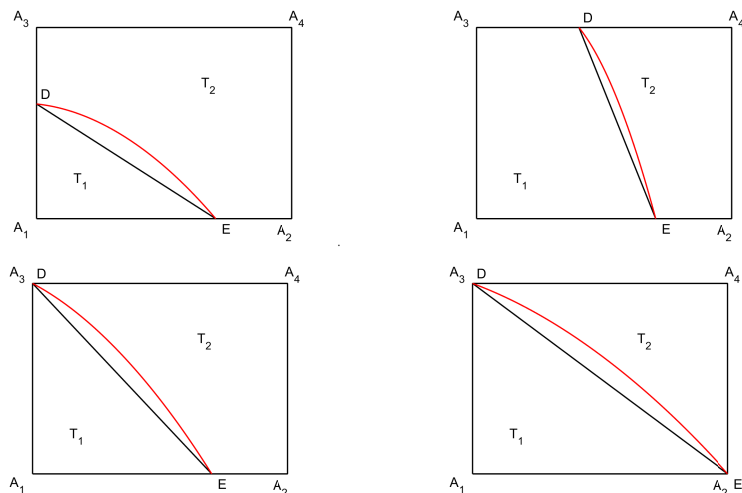$$(12) \qquad \hat{X} = G(X) = \mathbf{J}X + B$$

FIG. 2. *Reference interface elements of type* I, II, III, IV *(upper left to lower right).*

be the standard affine mapping from an arbitrary element T to the reference element $\hat{T}$ such that $\hat{A}_i = G(A_i)$, $i = 1, 2, 3, 4$. We further note that each interface element T is mapped into a reference element of the same type, where $\hat{E} = G(E)$ and $\hat{D} = G(D)$ and $\overline{\hat{D}\hat{E}} = G(\overline{DE})$. Furthermore, the interface points are $\hat{E} = G(E)$ and $\hat{D} = G(D)$. Each interface element is mapped into one of the four reference elements shown in Figure 2 where we omitted the $\hat{\ }$.

In order to construct piecewise polynomial IFE functions on the reference square elements, we need to map the jump conditions to the reference squares. For instance, the interface jump conditions (8) are applied to a piecewise polynomial bilinear pressure $\hat{p}$ on $\hat{\Gamma} = G(\Gamma \cap T)$:

$$[\hat{p}]_{\hat{\Gamma}} = 0, \qquad \left[\frac{1}{\rho}\,\boldsymbol{\nu} \cdot \hat{\nabla}\hat{p}\right]_{\hat{\Gamma}} = 0,$$

where $\hat{\nabla}\hat{p} = (\partial_{\hat{x}}\hat{p}, \partial_{\hat{y}}\hat{p})^t$ and $\hat{\boldsymbol{\nu}}$ is normal to $\hat{\Gamma}$. The other interface conditions are transformed to $\hat{T}$ in a similar manner.

Next, we describe an algorithm for constructing bilinear IFE shape functions $p^{(i)}$, $i = 1, 2, 3, 4$, of Lagrange type for the pressure by defining the IFE space on an arbitrary interface element $T = T_1 \cup T_2$ as

$$\mathcal{R}_p^1(T) = \left\{U \mid U|_{T_l} \in Q_1,\ l = 1, 2,\ [U]_{\overline{DE}} = 0,\ \left[\frac{1}{\rho}\nabla U \cdot \boldsymbol{\nu}\right]_{\overline{DE}} = 0,\ \left[\frac{\partial^2 U}{\partial x \partial y}\right]_{\overline{DE}} = 0\right\},$$

equipped with a Lagrange-type IFE shape functions $p^{(i)}$, $i = 1, 2, 3, 4$.

If L_i, $i = 1, 2, 3, 4$, are the standard Lagrange bilinear shape functions on the reference element, we write the IFE Lagrange bilinear shape functions $p^{(i)}$ satisfying $p^{(i)}(A_j) = \delta_{ij}$ as

$$(13) \qquad p^{(i)} = L_i + \phi^{(0),i}, \quad \phi^{(0),i} = \begin{cases} \sum_{j \in \mathcal{I}_2} c_j L_j & \text{on } T_1, \\ \sum_{j \in \mathcal{I}_1} c_j L_j & \text{on } T_2, \end{cases} \quad i = 1, 2, 3, 4.$$

For instance, the coefficients c_1, c_2, c_3, c_4 for defining $p^{(i)}$ on an interface element
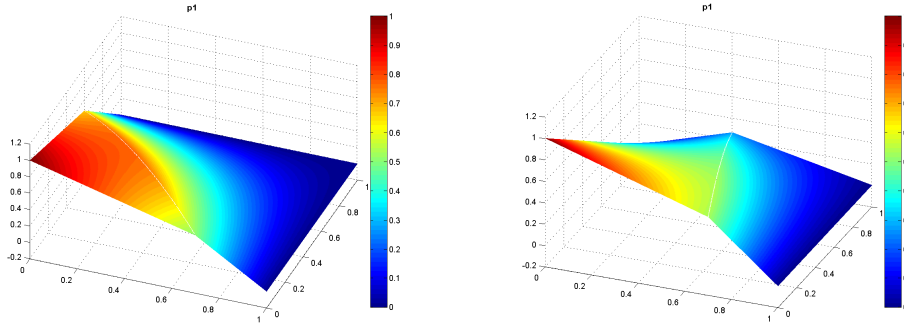
FIG. 3. *Lagrange bilinear IFE shape functions for the pressure on element of type* I *(left) and type* II *(right).*

of type I and II are determined by imposing the following four interface jump and consistency conditions:

$$(14a) \qquad p_1^{(i)}(D) - p_2^{(i)}(D) = 0, \qquad p_1^{(i)}(E) - p_2^{(i)}(E) = 0,$$

$$(14b) \quad \frac{1}{\rho_1} \frac{\partial p_1^{(i)}}{\partial \boldsymbol{\nu}} \left(\frac{D+E}{2} \right) - \frac{1}{\rho_2} \frac{\partial p_2^{(i)}}{\partial \boldsymbol{\nu}} \left(\frac{D+E}{2} \right) = 0, \quad \frac{\partial^2 p_1^{(i)}}{\partial x \partial y}(E) - \frac{\partial^2 p_2^{(i)}}{\partial x \partial y}(E) = 0.$$

The resulting 4×4 square linear systems yield a unique set of IFE shape functions [1, 3] with the following properties: (i) if $\rho_1 = \rho_2$ the IFE shape functions become the standard bilinear Lagrange shape functions; (ii) they yield finite element interpolants and solutions with optimal convergence rates under quasi-uniform mesh refinement; and (iii) they form a partition of unity. For an illustration of typical bilinear IFE shape functions for the pressure on interface elements of type I with $D = (0, 0.6)$, $E = (0.7, 0)$ and type II with $D = (0.4, 1)$, $E = (0.7, 0)$ using the parameters $\rho_1 = 1$, $c_1 = 1$, $\rho_2 = 15$, and $c_2 = 20$; see Figure 3.

Next, we define the bilinear IFE space for the velocity as

$$\mathcal{R}_{\mathbf{v}}^1(T) = \left\{ V \mid V|_{T_i} \in (Q_1)^2, \ [V \cdot \boldsymbol{\nu}]_{\overline{DE}} = 0, \ [\rho c^2 \nabla \cdot V]_{\overline{DE}} = 0, \left[\frac{\partial^2 V}{\partial x \partial y} \right]_{\overline{DE}} = 0 \right\}.$$

We now construct bilinear immersed shape functions for the velocity $\mathbf{v} = (u, v)^t$ by writing the standard bilinear Lagrange shape functions for $(Q_1)^2$ as $\mathbf{L}^{(i),l} = L_i \mathbf{e}_l$, $i = 1, 2, 3, 4$, $l = 1, 2$, where $\mathbf{e}_l$, $l = 1, 2$, are the canonical vectors in $\mathbb{R}^2$.

On the reference interface element $T = T_1 \cup T_2$ of type I shown in Figure 2 we write Lagrange IFE shape functions $\mathbf{v}^{(i),m}, i = 1, 2, 3, 4$, $m = 1, 2$, satisfying $\mathbf{v}^{(i),l}(A_j) = \delta_{ij} \mathbf{e}_l$ as

$$(15) \qquad \mathbf{v}^{(i),m} = \mathbf{L}^{(i),m} + \boldsymbol{\psi}^{(0),i}, \qquad \boldsymbol{\psi}^{(0),i} = \begin{cases} \sum_{l=1}^{2} \sum_{j \in \mathcal{I}_2} c^{(j),l} \mathbf{L}^{(j),l} & \text{on } T_1, \\ \sum_{l=1}^{2} \sum_{j \in \mathcal{I}_1} c^{(j),l} \mathbf{L}^{(j),l} & \text{on } T_2. \end{cases}$$

We determine the coefficients of $\mathbf{v}^{(i),m}$ on an interface element of types I and II by

imposing the interface and consistency conditions

$$\text{(16a)} \quad \mathbf{v}_1^{(i),m} \cdot \boldsymbol{\nu}(D) - \mathbf{v}_2^{(i),m} \cdot \boldsymbol{\nu}(D) = 0, \quad \mathbf{v}_1^{(i),m} \cdot \boldsymbol{\nu}(E) - \mathbf{v}_2^{(i),m} \cdot \boldsymbol{\nu}(E) = 0,$$

$$\text{(16b)} \quad \rho_1 c_1^2 \nabla \cdot \mathbf{v}_1^{(i),m}\left(\frac{D+E}{2}\right) - \rho_2 c_2^2 \nabla \cdot \mathbf{v}_2^{(i),m}\left(\frac{D+E}{2}\right) = 0,$$

$$\text{(16c)} \quad \frac{\partial^2 \mathbf{v}_1^{(i),m}}{\partial x \partial y}(D) - \frac{\partial^2 \mathbf{v}_2^{(i),m}}{\partial x \partial y}(D) = 0.$$

On interface elements of types I and II, the interface conditions (16) for each shape function $\mathbf{v}^{(i),m}$ lead to a rectangular system of 5 linear equations and 8 coefficients $\mathbf{c} = [c^{(1),1}, c^{(2),1}, c^{(3),1}, c^{(4),1}, c^{(1),2}, c^{(2),2}, c^{(3),2}, c^{(4),2}]^t$ written as $\mathbf{Mc} = \mathbf{b}$. On the reference element of type III, one of conditions (16a) is automatically satisified, thus dropped, yielding a 4×6 matrix $\mathbf{M}$ with $\mathbf{c} = [c^{(1),1}, c^{(2),1}, c^{(4),1}, c^{(1),2}, c^{(2),2}, c^{(4),2}]^t$. Similarly, on the reference element of type IV both jump conditions (16a) are dropped leading to a 3×4 matrix $\mathbf{M}$ with $\mathbf{c} = [c^{(1),1}, c^{(4),1}, c^{(1),2}, c^{(4),2}]^t$. In the remainder of this manuscript we denote the nullity of $\mathbf{M}$ by N_b and prove in the following theorem that $\mathbf{M}$ is full row rank for bilinear IFE spaces.

THEOREM 3.1. *The bilinear IFE shape functions for the velocity defined on reference interface elements by* (15) *and* (16) *lead to a linear system* $\mathbf{Mc} = \mathbf{b}$ *with a full row rank matrix.*

Proof. On the reference interface element $[0,1]^2$ of type I such that $D = (0,b)$ and $E = (a,0)$, $0 < a, b < 1$, the matrix $\mathbf{M} \in \mathbb{R}^{5 \times 8}$ with $r = \frac{\rho_1 c_1^2}{\rho_2 c_2^2}$ is given as

$$\text{(17)} \quad \mathbf{M} = \begin{bmatrix} b(b-1) & 0 & b^2 & 0 & a(b-1) & 0 & ab & 0 \\ b(a-1) & ab & 0 & 0 & a(a-1) & a^2 & 0 & 0 \\ 1 - \frac{b}{2} & -r(\frac{b}{2}-1) & -\frac{br}{2} & \frac{br}{2} & 1 - \frac{a}{2} & -\frac{ar}{2} & -r(\frac{a}{2}-1) & \frac{ar}{2} \\ -1 & -1 & -1 & 1 & 0 & 0 & 0 & 0 \\ 0 & 0 & 0 & 0 & -1 & -1 & -1 & 1 \end{bmatrix}$$

with $det(\mathbf{M}(:, [2,3,4,6,7])) = ab^2 r(a+b) > 0$ for $a > 0$, $b > 0$ which shows that $\mathbf{M}$ is full rank.

On the reference interface element of type II such that $D = (b,1)$ and $E = (a,0)$, $0 < a, b < 1$, the matrix $\mathbf{M} \in \mathbb{R}^{5 \times 8}$ is given [30]. A direct computation yields $det(\mathbf{M}(:, [1,2,3,5,6])) = (b-1)(ar+1-a) < 0$ which establishes that $\mathbf{M}$ is full row rank.

On a reference interface element of type III with $D = (0,1)$ and $E = (a,0)$, $0 < a < 1$, the matrix $\mathbf{M} \in \mathbb{R}^{4 \times 6}$ and $det(\mathbf{M}(:, [1,2,3,4])) = (a + r(2-a))/2 > 0$ which proves that $\mathbf{M}$ is full row rank.

Finally, we consider the reference interface element of type IV with $D = (0,1)$ and $E = (1,0)$, where the matrix $\mathbf{M} \in \mathbb{R}^{3 \times 4}$ and $det(\mathbf{M}(:, [1,2,3])) = -(1+r)/2 < 0$ which proves that $\mathbf{M}$ is full row rank. $\square$

For instance, on elements of types I and II the nullity of $\mathbf{M}$ is $N_b = 3$ and the solution set of $\mathbf{Mc} = \mathbf{b}$ is $\mathbf{c}^{(0)} + span\{\mathbf{c}^{(1)}, \mathbf{c}^{(2)}, \mathbf{c}^{(3)}\}$, where $\mathbf{c}^{(0)} = \mathbf{M}^t(\mathbf{MM}^t)^{-1}\mathbf{b}$ is the minimum-norm particular solution and $\mathbf{c}^{(j)}$, $j = 1, 2, 3$, is a basis of the null space of $\mathbf{M}$.

Now we construct the IFE shape functions for the velocity by following these steps:

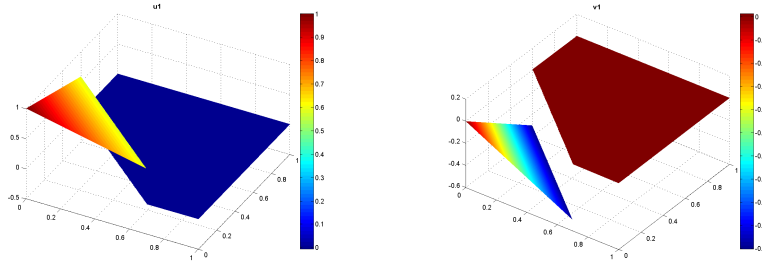1. Find a basis $\mathbf{c}^{(1)}, \mathbf{c}^{(2)}, \mathbf{c}^{(3)}$ of the null space of $\mathbf{M}$.

FIG. 4. *Lagrange bilinear IFE shape functions for the velocity on element of type I.*

2. Compute the minimum-norm particular solution $\mathbf{c}^{(0)}$ of $\mathbf{Mc} = \mathbf{b}$ for each of the eight IFE shape functions.
3. Replace the coefficients in (15) by the minimum-norm solutions $\mathbf{c}^{(0)}$ for each vertex to obtain eight IFE shape functions $\mathbf{v}^{(i),m}$, $i = 1, 2, 3, 4$, $m = 1, 2$.
4. Substitute the coefficients $\mathbf{c}^{(1)}$, $\mathbf{c}^{(2)}$, and $\mathbf{c}^{(3)}$ in $\boldsymbol{\psi}^{(0),i}$ (see (15)) to obtain three additional "bubble" IFE functions, $\mathbf{w}^{(1)}$, $\mathbf{w}^{(2)}$, and $\mathbf{w}^{(3)}$ such that $\mathbf{w}^{(i)}(A_j) = 0, j = 1, 2, 3, 4$, $i = 1, 2, 3$.

Thus, the bilinear IFE space for the velocity is

$$\mathcal{R}^1_{\mathbf{v}}(T) = span\{\mathbf{v}^{(i),m}, \ i = 1, 2, 3, 4, \ m = 1, 2, \ \mathbf{w}^{(1)}, \mathbf{w}^{(2)}, \mathbf{w}^{(3)}\}.$$

Elements of types III and IV are treated in a similar manner.

A typical bilinear IFE shape function for the velocity on interface elements of type I with $D = (0, 0.6)$, $E = (0.7, 0)$ using the parameters $\rho_1 = 1$, $c_1 = 1$, $\rho_2 = 15$, and $c_2 = 20$ is plotted in Figure 4.

We note that the IFE functions for the pressure are continuous while those for the velocity are discontinuous across the interface which is consistent with the true solutions.

In order to construct biquadratic IFE shape functions for the pressure we order the Q_2 vertices A_{ij} as $Z_1, Z_2, \ldots, Z_9$ and consider the associated standard Lagrange Q_2 shape functions $L_1, L_2, \ldots, L_9$, where $L_i(Z_j) = \delta_{ij}$. Without loss of generality, we consider an interface element $T = T_1 \cup T_2$ such that no vertex is on the interface and define new sets $\mathcal{I}_1$ and $\mathcal{I}_2$ such that $\mathcal{I}_1 \cup \mathcal{I}_2 = \{1, 2, \ldots, 9\}$. Assume that the curved interface $\widetilde{DE}$ is parameterized by $t \to X(t) = (x_1(t), x_2(t))$, $t = [0, 1]$, where $X(0) = D$ and $X(1) = E$; we define 3 interface points $X_s = X(\xi_s)$, $s = 0, 1, 2$, and ξ_s are the roots of Legendre polynomial of degree 3 shifted to [0,1].

The biquadratic Lagrange IFE shape functions for the pressure are written as

$$(18) \qquad p^{(i)} = L_i + \phi^{(0),i}, \quad \phi^{(0),i} = \begin{cases} \sum_{j \in \mathcal{I}_2} c_j L_j & \text{on } T_1, \\ \sum_{j \in \mathcal{I}_1} c_j L_j & \text{on } T_2, \end{cases} \quad i = 1, 2, \ldots, 9,$$

where coefficients $c_1, c_2, \ldots, c_9$ for $p^{(i)}$ are determined by imposing the following interface jump and consistency conditions:

$$[p^{(i)}](X_0) = 0, \ [p^{(i)}](X_1) = 0, \ [p^{(i)}](X_2) = 0,$$

$$\left[\frac{1}{\rho}\nabla p^{(i)} \cdot \boldsymbol{\nu}\right](X_0) = 0, \ \left[\frac{1}{\rho}\nabla p^{(i)} \cdot \boldsymbol{\nu}\right](X_2) = 0, \ [c^2\Delta p^{(i)}](X_1) = 0,$$

$$\left[\frac{\partial^3 p^{(i)}}{\partial^2 x \partial y}\right](X_1) = 0, \left[\frac{\partial^3 p^{(i)}}{\partial x \partial^2 y}\right](X_1) = 0, \left[\frac{\partial^4 p^{(i)}}{\partial^2 x \partial^2 y}\right](X_1) = 0.$$

Next let $\mathbf{L}^{(j),l}$, $j = 1, 2, \ldots, 9$, $l = 1, 2$, denote the standard biquadratic shape functions for the velocity and write the corresponding IFE shape functions as

$$\mathbf{v}^{(i),m} = \mathbf{L}^{(i),m} + \boldsymbol{\psi}^{(0),i}, \ \ \boldsymbol{\psi}^{(0),i} = \begin{cases} \sum\limits_{l=1}^{2} \sum\limits_{j \in \mathcal{I}_2} c^{(j),l}\mathbf{L}^{(j),l} & \text{on } T_1, \\ \sum\limits_{l=1}^{2} \sum\limits_{j \in \mathcal{I}_1} c^{(j),l}\mathbf{L}^{(j),l} & \text{on } T_2, \end{cases} \ \ \begin{matrix} j = 1, 2, \ldots, 9, \\ m = 1, 2. \end{matrix}$$

The coefficients $c^{(j),l}$, $j = 1, 2, \ldots, 9$, $l = 1, 2$, are computed by imposing the following interface conditions:

(19a) $\qquad [\mathbf{v}^{(i),m} \cdot \boldsymbol{\nu}](X_0) = 0, \ [\mathbf{v}^{(i),m} \cdot \boldsymbol{\nu}](X_1) = 0, \ [\mathbf{v}^{(i),m} \cdot \boldsymbol{\nu}](X_2) = 0,$

(19b) $[\rho c^2 (\nabla \cdot \mathbf{v}^{(i),m})](X_0) = 0, \ [\rho c^2 (\nabla \cdot \mathbf{v}^{(i),m})](X_2) = 0, \ [c^2 (\triangle \mathbf{v}^{(i),m}) \cdot \boldsymbol{\nu}](X_1) = 0,$

(19c) $\qquad \left[\dfrac{\partial^3 u^{(i),m}}{\partial^2 x \partial y}\right](X_1) = 0, \ \left[\dfrac{\partial^3 u^{(i),m}}{\partial x \partial^2 y}\right](X_1) = 0, \ \left[\dfrac{\partial^4 u^{(i),m}}{\partial^2 x \partial^2 y}\right](X_1) = 0,$

(19d) $\qquad \left[\dfrac{\partial^3 v^{(i),m}}{\partial^2 x \partial y}\right](X_1) = 0, \ \left[\dfrac{\partial^3 v^{(i),m}}{\partial x \partial^2 y}\right](X_1) = 0, \ \left[\dfrac{\partial^4 v^{(i),m}}{\partial^2 x \partial^2 y}\right](X_1) = 0.$

Following the procedure for bilinear IFE shape functions, on types I and II elements, we obtain 18 biquadartic Lagrange shape functions $\mathbf{v}^{(i),m}, i = 1, 2, \ldots, 9, m = 1, 2$, and $N_b = 6$ bubble IFE shape functions $\mathbf{w}^{(i)}, i = 1, 2, \ldots, 6$. We note that the resulting biquadratic IFE space for the velocity is bigger than the standard Q_2 space.

Now we are ready to define a global bilinear ($k = 1$) and biquadratic ($k = 2$) immersed discontinuous finite element spaces as

(20) $\qquad \mathcal{U}_h^k = \{\mathbf{U}_h \mid \mathbf{U}_h|_T \ (Q_k)^3, \ T \in \mathcal{T}_h^S, \ \mathbf{U}_h|_T \in \mathcal{R}_p^k(T) \times \mathcal{R}_{\mathbf{v}}^k(T), \ T \in \mathcal{T}_h^I\},$

where all functions $\mathbf{U}_h$ are fully discontinuous across element boundaries. Furthermore, the IFE shape functions are discontinuous across physical interfaces yielding a discontinuous $\mathbf{U}_h$ across the interface. We also use the local spaces

(21) $\qquad \mathcal{U}_h^k(T) = \begin{cases} (Q_k)^3 & for \ T \in \mathcal{T}_h^S, \\ \mathcal{R}_p^k(T) \times \mathcal{R}_{\mathbf{v}}^k(T) & for \ T \in \mathcal{T}_h^I, \end{cases} \qquad k = 1, 2.$

The true solution $\mathbf{U}$ of (2a) is approximated by $\mathbf{U}_h \in \mathcal{U}_h^k$ such that $\mathbf{U}|_T \approx \mathbf{U}_h|_T = [p_h^T, (\mathbf{v}_h^T)^t]^t$, where

(22a) $\qquad p_h^T = \begin{cases} \sum\limits_{i=1}^{(k+1)^2} c^{(i)}(t)L_i(x, y) & for \ T \in \mathcal{T}_h^S, \\ \sum\limits_{i=1}^{(k+1)^2} c^{(i)}(t)p^{(i)}(x, y) & for \ T \in \mathcal{T}_h^I, \end{cases}$

(22b) $\qquad \mathbf{v}_h^T = \begin{cases} \sum\limits_{l=1}^{2} \sum\limits_{i=1}^{(k+1)^2} c^{(i),l}(t)\mathbf{L}^{(i),l}(x, y) & for \ T \in \mathcal{T}_h^S, \\ \sum\limits_{l=1}^{2} \sum\limits_{i=1}^{(k+1)^2} c^{(i),l}(t)\mathbf{v}^{(i),l}(x, y) + \sum\limits_{i=1}^{N_b} d^{(i)}(t)\mathbf{w}^{(i)}(x, y) & for \ T \in \mathcal{T}_h^I, \end{cases}$

where $N_b = 3$ for bilinear IFE spaces and $N_b = 6$ for biquadratic IFE spaces.

IFE velocity spaces with curl-free condition. For acoustic problems subjected to curl-free initial velocity, i.e., $\nabla \times \mathbf{v}(x, y, 0) = 0$ on $\tilde{\Omega}$, one can apply the curl operator to the second equation in (1a) to obtain the following involution condition

$$(23) \qquad \nabla \times \mathbf{v} = 0 \quad \text{for all } (x, y) \in \tilde{\Omega}, \text{ and } t \geq 0,$$

which, by differentiation, yields for $j \geq 0$

$$(24) \qquad \left[\frac{\partial^j(\nabla \times \mathbf{v})}{\partial x^l \partial y^{j-l}}\right]_\Gamma = 0, \ 0 \leq l \leq j, \quad \text{for all } (x, y) \in \Gamma \text{ and } t \geq 0.$$

Let us note that since the tangential component of $\mathbf{v}$ is discontinuous at the interface, $\nabla \times \mathbf{v}$ is not defined on Γ.

The "curl-free" interface conditions (24) are neither required for the construction of our IFE spaces nor for the stability of the IDG method. They are used to obtain smaller IFE velocity spaces yielding a more efficient algorithm.

For instance, each bilinear IFE velocity function $\mathbf{v}^{i,m} \in \mathcal{R}_{\mathbf{v}}^{1,cf}(T)$ given by (15) satisfies (16) and

$$(25) \quad \left(\frac{\partial u_1^{(i),m}}{\partial y} - \frac{\partial v_1^{(i),m}}{\partial x}\right)\left(\frac{D+E}{2}\right) - \left(\frac{\partial u_2^{(i),m}}{\partial y} - \frac{\partial v_2^{(i),m}}{\partial x}\right)\left(\frac{D+E}{2}\right) = 0.$$

Similarly, each biquadratic IFE velocity function $\mathbf{v}^{(i),m} \in \mathcal{R}_{\mathbf{v}}^{2,cf}(T)$ satisfies (19) and the curl-free jump conditions

$$(26) \quad [\nabla \times \mathbf{v}^{(i),m}](X_1) = 0, \ \left[\frac{\partial(\nabla \times \mathbf{v}^{(i),m})}{\partial x}\right](X_1) = 0, \ \left[\frac{\partial(\nabla \times \mathbf{v}^{(i),m})}{\partial y}\right](X_1) = 0.$$

The resulting $\mathcal{R}_{\mathbf{v}}^{2,cf}(T)$ space has dimension 21 which is smaller than the dimension of $\mathcal{R}_{\mathbf{v}}^{2}(T)$. As for $\mathcal{U}_h^k$ in (21) we use $\mathcal{R}_{\mathbf{v}}^{k,cf}(T)$ to define smaller global IFE spaces $\mathcal{U}_h^{k,cf}$, $k = 1, 2$, satisfying the curl-free jumps.

4. IDG methods. In [30] we investigated the following two DG formulations to solve the acoustic interface problem (2): (i) a standard DG formulation obtained by testing (2a) against $\mathbf{V}$ leading to an unstable method and (ii) weighted IDG and IDG-NI formulations obtained by testing (2a) against the function $\mathbf{SV}$ leading to stable methods. In this manuscript we derive and study both the IDG and IDG-NI methods.

For our problem we let $\mathbf{S}$ be a piecewise constant matrix such that

$$\mathbf{S}|_{\Omega_i} = \mathbf{S}_i = \begin{pmatrix} \frac{1}{\rho_i c_i^2} & 0 & 0 \\ 0 & \rho_i & 0 \\ 0 & 0 & \rho_i \end{pmatrix}, \tilde{\mathbf{A}} = \mathbf{SA} = \begin{pmatrix} 0 & 1 & 0 \\ 1 & 0 & 0 \\ 0 & 0 & 0 \end{pmatrix}, \ \tilde{\mathbf{B}} = \mathbf{SB} = \begin{pmatrix} 0 & 0 & 1 \\ 0 & 0 & 0 \\ 1 & 0 & 0 \end{pmatrix}.$$

In order to obtain the discrete weak IDG formulation, (i) we replace $\mathbf{U}$ by $\mathbf{U}_h \in \mathcal{U}_h^k$ and $\mathbf{V}$ by $\mathbf{V}_h \in \mathcal{U}_h^k$, $k = 1, 2$, or replace $\mathbf{U}$ by $\mathbf{U}_h \in \mathcal{U}_h^{k,cf}$ and $\mathbf{V}$ by $\mathbf{V}_h \in \mathcal{U}_h^{k,cf}$, $k = 1, 2$, for curl-free velocity and (ii) apply on element boundaries the numerical flux

$$(27a) \qquad \widehat{\mathbf{D}(\mathbf{n})\mathbf{U}}_h = \mathbf{F}^c(\mathbf{U}_h^-, \mathbf{U}_h^+) + \mathbf{F}^u(\mathbf{U}_h^-, \mathbf{U}_h^+),$$

(27b)
$$\mathbf{F}^c(\mathbf{U}_h^-, \mathbf{U}_h^+) = \frac{1}{2}\mathbf{D}(\mathbf{n})(\mathbf{U}_h^+ + \mathbf{U}_h^-), \ \mathbf{F}^u(\mathbf{U}_h^-, \mathbf{U}_h^+) = -\frac{1}{2}(1-\beta)|\mathbf{D}(\mathbf{n})|(\mathbf{U}_h^- - \mathbf{U}_h^+),$$

where $\mathbf{D}(\mathbf{n}) = \mathbf{A}n_x + \mathbf{B}n_y$ and $\mathbf{n} = (n_x, n_y)^t$ is the unit outward normal vector on the boundary of an element T and $0 \le \beta \le 1$. We select $\beta = 1$ for the central flux, $\beta = 0.5$ for the partial upwinding, and $\beta = 0$ for full upwinding. The full upwinding flux is used for our numerical examples except when indicated otherwise. The standard notation $\mathbf{U}_h^\pm(\mathbf{x}) = \lim_{\epsilon \to 0^\pm} \mathbf{U}_h(\mathbf{x} - \epsilon\mathbf{n})$ is used.

Thus the IDG formulation on a noninterface element T for $\mathbf{U}_h$ is

(28a) $$\int_T \mathbf{V}_h^t \mathbf{S}\frac{\partial \mathbf{U}_h}{\partial t}dxdy + \mathcal{A}_T^{S,c}(\mathbf{V}_h, \mathbf{U}_h) + \mathcal{A}_T^u(\mathbf{V}_h, \mathbf{U}_h) = 0 \quad \forall \ \mathbf{V}_h \in (Q_k)^3,$$

(28b) $$\mathcal{A}_T^{S,c}(\mathbf{V}_h, \mathbf{U}_h) = -\int_T \mathbf{U}_h^t L(\mathbf{V}_h)dxdy + \int_{\partial T} \mathbf{V}_h^{+^t}\mathbf{S}\mathbf{F}^c(\mathbf{U}_h^-, \mathbf{U}_h^+)ds,$$

(28c) $$\mathcal{A}_T^u(\mathbf{V}_h, \mathbf{U}_h) = \int_{\partial T} \mathbf{V}_h^{+^t}\mathbf{S}\mathbf{F}^u(\mathbf{U}_h^-, \mathbf{U}_h^+)ds,$$

where $L(\mathbf{V}) = \tilde{\mathbf{A}}\frac{\partial \mathbf{V}}{\partial x} + \tilde{\mathbf{B}}\frac{\partial \mathbf{V}}{\partial y}$.

On an interface element cut by the interface Γ into T_1 and T_2 and $T = T_1 \cup T_2$ as illustrated in Figure 2, where $\Gamma_3 = \overline{DE}$ for bilinear IFE spaces and $\Gamma_3 = \widetilde{DE} = T \cap \Gamma$ for biquadratic IFE spaces, we write the weak formulation for $\mathbf{U}_h$ as

(29a) $$\int_{T_1} \mathbf{V}_{1,h}^t \mathbf{S}_1 \frac{\partial \mathbf{U}_{1,h}}{\partial t}dxdy + \int_{T_2} \mathbf{V}_{2,h}^t \mathbf{S}_2 \frac{\partial \mathbf{U}_{2,h}}{\partial t}dxdy + \mathcal{A}_T^{I,c}(\mathbf{V}_h, \mathbf{U}_h)$$
$$+ \mathcal{A}_T^u(\mathbf{V}_h, \mathbf{U}_h) = 0,$$

(29b) $$\mathcal{A}_T^{I,c}(\mathbf{V}_h, \mathbf{U}_h) = \int_{\partial T} \mathbf{V}_h^{+^t}\mathbf{S}\mathbf{F}^c(U_h^-, \mathbf{U}_h^+)ds - \int_T \mathbf{U}_h^t L(\mathbf{V}_h)dxdy + \frac{1}{2}\mathcal{B}_T^I(\mathbf{V}_h, \mathbf{U}_h),$$

(29c) $$\mathcal{B}_T^I(\mathbf{V}_h, \mathbf{U}_h) = \int_{\Gamma_3} [\mathbf{V}_{1,h}^t(\nu_x\tilde{\mathbf{A}} + \nu_y\tilde{\mathbf{B}})\mathbf{U}_{1,h}ds - \mathbf{V}_{2,h}^t(\nu_x\tilde{\mathbf{A}} + \nu_y\tilde{\mathbf{B}})\mathbf{U}_{2,h}]ds.$$

Here let us make the following remarks:
1. The same upwind terms $\mathcal{A}_T^u$ are used on all elements.
2. For biquadratic IFE spaces built on elements cut by a curved interface, the jump conditions are enforced at a set of points. Thus, the jump term $\mathcal{B}_T(\mathbf{V}_h, \mathbf{U}_h)$ across the interface is not zero and may cause numerical instability. We remedied this by adding the stabilizing term $-\frac{1}{2}\mathcal{B}_T^I(\mathbf{V}_h, \mathbf{U}_h)$ to obtain (29).

Summing (28) over all noninterface elements and (29) over all interface elements, we obtain a stable IDG formulation for each of the four IFE spaces $\mathcal{U}_h^k$, $k = 1, 2$ and $\mathcal{U}_h^{k,cf}$, $k = 1, 2$. For simplicity, we only write the IDG formulation for $\mathbf{U}_h \in \mathcal{U}_h^k$ such that

(30a) $$\sum_{T \in \mathcal{T}_h} \int_T \mathbf{V}_h^t \mathbf{S}\mathbf{U}_{h,t} + \mathcal{A}^c(\mathbf{V}_h, \mathbf{U}_h) + \mathcal{A}^u(\mathbf{V}_h, \mathbf{U}_h) = 0 \ \forall \ \mathbf{V}_h \in \mathcal{U}_h^k,$$

(30b) $$\mathcal{A}^c(\mathbf{V}_h, \mathbf{U}_h) = \sum_{T \in \mathcal{T}_h^S} \mathcal{A}_T^{S,c}(\mathbf{V}_h, \mathbf{U}_h) + \sum_{T \in \mathcal{T}_h^I} \mathcal{A}_T^{I,c}(\mathbf{V}_h, \mathbf{U}_h),$$

(30c) $$\mathcal{A}^u(\mathbf{V}_h, \mathbf{U}_h) = \sum_{T \in \mathcal{T}_h} \mathcal{A}_T^u(\mathbf{V}_h, \mathbf{U}_h).$$

We start by proving a stability result for the problem (2).

THEOREM 4.1. *Let* $\mathbf{U}$ *be the true solution of the acoustic interface problem* (2) *defined on* $\Omega = \Omega_1 \cup \Omega_2$ *such that* $\overline{\Omega} = \overline{\Omega_1 \cup \Omega_2}$ *satisfying periodic boundary conditions on* $\partial\Omega$ *and jump conditions* (1b) *across the interface. Then we have*

$$\text{(31a)} \qquad\qquad \mathcal{E}(t) = \mathcal{E}(0) \text{ for all } t \geq 0,$$

$$\text{(31b)} \qquad\qquad \mathcal{E}(t) = \frac{1}{2}\sum_{i=1}^{2}\int_{\Omega_i}\mathbf{U}_i^t(x,y,t)\mathbf{S}_i\mathbf{U}_i(x,y,t)dxdy.$$

Proof. Multiplying (2a) by $\mathbf{SU}$ and integrating over $\Omega = \Omega_1 \cup \Omega_2$ we obtain

$$\int_{\Omega_1}\mathbf{U}_1^t\mathbf{S}_1\frac{\partial\mathbf{U}_1}{\partial t}dxdy + \int_{\Omega_2}\mathbf{U}_2^t\mathbf{S}_2\frac{\partial\mathbf{U}_2}{\partial t}dxdy + \int_{\Omega_1}\mathbf{U}_1^t\tilde{\mathbf{A}}\frac{\partial\mathbf{U}_1}{\partial x}dxdy$$

$$\text{(32)}\qquad + \int_{\Omega_1}\mathbf{U}_1^t\tilde{\mathbf{B}}\frac{\partial\mathbf{U}_1}{\partial y}dxdy + \int_{\Omega_2}\mathbf{U}_2^t\tilde{\mathbf{A}}\frac{\partial\mathbf{U}_2}{\partial x}dxdy + \int_{\Omega_2}\mathbf{U}_2^t\tilde{\mathbf{B}}\frac{\partial\mathbf{U}_2}{\partial y}dxdy = 0,$$

which can be written as

$$\frac{1}{2}\frac{d}{dt}\left(\int_{\Omega_1}\mathbf{U}_1^t\mathbf{S}_1\mathbf{U}_1 dxdy + \int_{\Omega_2}\mathbf{U}_2^t\mathbf{S}_2\mathbf{U}_2 dxdy\right)$$

$$+ \frac{1}{2}\int_{\Omega_1}\left(\frac{\partial}{\partial x}\mathbf{U}_1^t\tilde{\mathbf{A}}\mathbf{U}_1 + \frac{\partial}{\partial y}\mathbf{U}_1^t\tilde{\mathbf{B}}\mathbf{U}_1\right)dxdy$$

$$\text{(33)}\qquad + \frac{1}{2}\int_{\Omega_2}\left(\frac{\partial}{\partial x}\mathbf{U}_2^t\tilde{\mathbf{A}}\mathbf{U}_2 + \frac{\partial}{\partial y}\mathbf{U}_2^t\tilde{\mathbf{B}}\mathbf{U}_2\right)dxdy = 0.$$

Applying the divergence theorem yields

$$\frac{1}{2}\frac{d}{dt}\left(\int_{\Omega_1}\mathbf{U}_1^t\mathbf{S}_1\mathbf{U}_1 dxdy + \int_{\Omega_2}\mathbf{U}_2^t\mathbf{S}_2\mathbf{U}_2 dxdy\right) + \frac{1}{2}\int_{\partial\Omega_1\backslash\Gamma}\mathbf{U}_1^t(n_{1x}\tilde{\mathbf{A}} + n_{1y}\tilde{\mathbf{B}})\mathbf{U}_1 ds$$

$$+ \frac{1}{2}\int_{\partial\Omega_2\backslash\Gamma}\mathbf{U}_2^t(n_{2x}\tilde{\mathbf{A}} + n_{2y}\tilde{\mathbf{B}})\mathbf{U}_2 ds + \frac{1}{2}\int_{\Gamma}\mathbf{U}_1^t(n_{1x}\tilde{\mathbf{A}} + n_{1x}\tilde{\mathbf{B}})\mathbf{U}_1 ds$$

$$\text{(34)}\qquad - \frac{1}{2}\int_{\Gamma}\mathbf{U}_2^t(n_{1x}\tilde{\mathbf{A}} + n_{1x}\tilde{\mathbf{B}})\mathbf{U}_2 ds = 0,$$

where $\boldsymbol{\nu}_1 = (n_{1x}, n_{1x})^t$ and $\boldsymbol{\nu}_2 = (n_{2x}, n_{2x})^t$, respectively, are outward unit normal vectors on the boundary of Ω_1, Ω_2. Here, we have used $\boldsymbol{\nu}_2 = -\boldsymbol{\nu}_1$ on Γ.

By the interface conditions (1b) we show that

$$\mathbf{U}_1^t(n_{1x}\tilde{\mathbf{A}} + n_{1y}\tilde{\mathbf{B}})\mathbf{U}_1\mid_\Gamma -\mathbf{U}_2^t(n_{1x}\tilde{\mathbf{A}} + n_{1y}\tilde{\mathbf{B}})\mathbf{U}_2\mid_\Gamma$$

$$\text{(35)}\qquad = 2p_1\mid_\Gamma(\mathbf{v}_1\cdot\boldsymbol{\nu}_1\mid_\Gamma) - 2p_2\mid_\Gamma(\mathbf{v}_2\cdot\boldsymbol{\nu}_1\mid_\Gamma) = 0.$$

Furthermore, by periodic boundary conditions we have

$$\text{(36)}\quad \frac{1}{2}\int_{\partial\Omega_1\backslash\Gamma}\mathbf{U}_1^t(n_{1x}\tilde{\mathbf{A}} + n_{1y}\tilde{\mathbf{B}})\mathbf{U}_1 ds + \frac{1}{2}\int_{\partial\Omega_2\backslash\Gamma}\mathbf{U}_2^t(n_{2x}\tilde{\mathbf{A}} + n_{2y}\tilde{\mathbf{B}})\mathbf{U}_2 ds = 0.$$

Combining (34), (35), and (36) yields $\frac{d}{dt}\mathcal{E}(t) = 0$. Integrating over $[0, t]$ completes the proof. $\square$

Before we state a stability result for the IDG solution we first prove that the bilinear form $\mathcal{A}^c$ is skew symmetric.
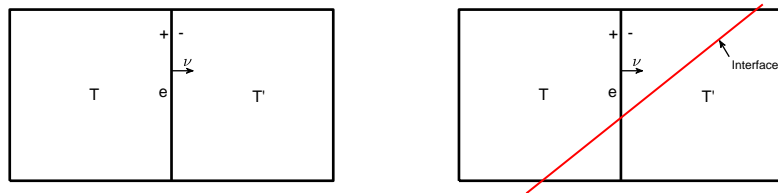
FIG. 5. *Adjacent noninterface (left) and interface (right) elements.*

LEMMA 4.2. *The bilinear form* $\mathcal{A}^c(\mathbf{V}_h, \mathbf{U}_h)$ *satisfies* $\mathcal{A}^c(\mathbf{V}_h, \mathbf{U}_h) = -\mathcal{A}^c(\mathbf{U}_h, \mathbf{V}_h)$ *for all* $\mathbf{V}_h$ *and* $\mathbf{U}_h$ *periodic functions in* $\mathcal{U}_h^k$ *or* $\mathcal{U}_h^{k,cf}$.

Proof. We consider two neighboring elements T and T' sharing an edge $e = \partial T \cap \partial T'$ as shown in Figure 5.

Let us use (28b) to define $\mathcal{A}_T^{S,c}(\mathbf{U}_h, \mathbf{V}_h)$ and $\mathcal{A}_{T'}^{S,c}(\mathbf{U}_h, \mathbf{V}_h)$ on noninterface elements T and T' and integrate by parts to have

$$
\mathcal{A}_T^{S,c}(\mathbf{U}_h, \mathbf{V}_h) = \int_T \mathbf{U}_h^t L(\mathbf{V}_h) dx dy
$$
$$
(37) \qquad - \int_{\partial T} \mathbf{U}_h^{+t} \mathbf{SD}(\boldsymbol{\nu}) \mathbf{V}_h^+ ds + \int_{\partial T} \mathbf{U}_h^{+t} \mathbf{SF}^c(\mathbf{V}_h^-, \mathbf{V}_h^+) ds
$$

and

$$
\mathcal{A}_{T'}^{S,c}(\mathbf{U}_h, \mathbf{V}_h) = \int_{T'} \mathbf{U}_h^t L(\mathbf{V}_h) dx dy
$$
$$
(38) \qquad - \int_{\partial T'} \mathbf{U}_h^{-t} \mathbf{SD}(-\boldsymbol{\nu}) \mathbf{V}_h^- ds + \int_{\partial T'} \mathbf{U}_h^{-t} \mathbf{SF}^c(\mathbf{V}_h^-, \mathbf{V}_h^+) ds.
$$

Adding (37) and (38) yields

$$
\mathcal{A}_{T \cup T'}^{S,c}(\mathbf{U}_h, \mathbf{V}_h) = \mathcal{A}_T^{S,c}(\mathbf{U}_h, \mathbf{V}_h) + \mathcal{A}_{T'}^{S,c}(\mathbf{U}_h, \mathbf{V}_h) = \int_{T \cup T'} \mathbf{U}_h^t L(\mathbf{V}_h) dx dy
$$
$$
- \int_{\partial T \backslash e} \mathbf{U}_h^{+t} \mathbf{SD}(\boldsymbol{\nu}) \mathbf{V}_h^+ ds + \int_{\partial T \backslash e} \mathbf{U}_h^{+t} \mathbf{SF}^c(\mathbf{V}_h^-, \mathbf{V}_h^+) ds
$$
$$
(39a) \quad - \int_{\partial T' \backslash e} \mathbf{U}_h^{-t} \mathbf{SD}(-\boldsymbol{\nu}) \mathbf{V}_h^- ds + \int_{\partial T' \backslash e} \mathbf{U}_h^{-t} \mathbf{SF}^c(\mathbf{V}_h^-, \mathbf{V}_h^+) ds + \mathcal{Q}_e,
$$

where

$$
\mathcal{Q}_e = - \int_e \mathbf{U}_h^{+t} \mathbf{SD}(\boldsymbol{\nu}) \mathbf{V}_h^+ ds + \int_e \mathbf{U}_h^{+t} \mathbf{SD}(\boldsymbol{\nu}) \frac{(\mathbf{V}_h^+ + \mathbf{V}_h^-)}{2} ds
$$
$$
- \int_e \mathbf{U}_h^{-t} \mathbf{SD}(-\boldsymbol{\nu}) \mathbf{V}_h^- ds + \int_e \mathbf{U}_h^{-t} \mathbf{SD}(-\boldsymbol{\nu}) \frac{(\mathbf{V}_h^+ + \mathbf{V}_h^-)}{2} ds,
$$
$$
(39b) \qquad = - \int_e \frac{(\mathbf{U}_h^+ + \mathbf{U}_h^-)^t}{2} \mathbf{SD}(\boldsymbol{\nu}) (\mathbf{V}_h^+ - \mathbf{V}_h^-) ds.
$$

Next, we consider two neighboring interface elements T and T' sharing an edge e cut by the interface as shown in Figure 5. By (29b) we define $\mathcal{A}_T^{I,c}(\mathbf{U}_h, \mathbf{V}_h)$ and

$\mathcal{A}_{T'}^{I;c}(\mathbf{U}_h, \mathbf{V}_h)$, integrate both terms by parts, and add the 2 terms to write

$$\mathcal{A}_{T \cup T'}^{I;c}(\mathbf{U}_h, \mathbf{V}_h) = \mathcal{A}_T^{I;c}(\mathbf{U}_h, \mathbf{V}_h) + \mathcal{A}_{T'}^{I;c}(\mathbf{U}_h, \mathbf{V}_h) = \int_{T \cup T'} \mathbf{U}_h^t L(\mathbf{V}_h) dx dy$$

$$- \int_{\partial T \setminus e} \mathbf{U}_h^{+\,t} \mathbf{S} \mathbf{D}(\boldsymbol{\nu}) \mathbf{V}_h^+ ds + \int_{\partial T \setminus e} \mathbf{U}_h^{+\,t} \mathbf{S} \mathbf{F}^c(\mathbf{V}_h^-, \mathbf{V}_h^+) ds$$

(40a) $$\qquad - \int_{\partial T' \setminus e} \mathbf{U}_h^{-\,t} \mathbf{S} \mathbf{D}(-\boldsymbol{\nu}) \mathbf{V}_h^- ds + \int_{\partial T' \setminus e} \mathbf{U}_h^{-\,t} \mathbf{S} \mathbf{F}^c(\mathbf{V}_h^-, \mathbf{V}_h^+) ds + \mathcal{Q}_e + \mathcal{Q}_\gamma,$$

where $\gamma = (T \cup T') \cap \Gamma$ and

(40b) $$\mathcal{Q}_\gamma = -\frac{1}{2} \mathcal{B}_T^I - \frac{1}{2} \mathcal{B}_{T'}^I.$$

Integrating $\mathcal{A}_T^{S,c}(\mathbf{U}_h, \mathbf{V}_h)$ and $\mathcal{A}_T^{I,c}(\mathbf{U}_h, \mathbf{V}_h)$ by parts, adding the contributions from all elements, using the formulas (39) and (40) for neighboring elements, and dropping the boundary terms on $\partial \Omega$ by perodicity we write

(41) $$\mathcal{A}^c(\mathbf{U}_h, \mathbf{V}_h) = \sum_{T \in \mathcal{T}_h^S} \mathcal{A}_T^{S,c}(\mathbf{U}_h, \mathbf{V}_h) + \sum_{T \in \mathcal{T}_h^I} \mathcal{A}_T^{I,c}(\mathbf{U}_h, \mathbf{V}_h),$$

(42) $$= \sum_{T \in \mathcal{T}_h} \int_T \mathbf{U}_h^t L(\mathbf{V}_h) dx dy + \sum_{e \in \mathcal{Z}_h^0} Q_e - \frac{1}{2} \sum_{T \in \mathcal{T}_h^I} \mathcal{B}_T^I,$$

where $\mathcal{Z}_h^0$ denotes the set of all interior edges in the mesh.   Finally, combining (28b), (29b), (30b) with the periodic boundary conditions to drop the terms on $\partial \Omega$ and show that $\mathcal{A}^c(\mathbf{V}_h, \mathbf{U}_h) = -\mathcal{A}^c(\mathbf{U}_h, \mathbf{V}_h)$. This completes the proof. $\qquad\square$

In the next theorem we state and prove our main stability result.

THEOREM 4.3. *Let $\mathbf{U}_h$ be the IDG solution of the acoustic problem* (2) *defined on Ω such that $\overline{\Omega} = \overline{\Omega_1 \cup \Omega_2}$ which is partitioned into a Cartesian mesh $\mathcal{T}_h$. If the true solution satisfies periodic boundary conditions on $\partial \Omega$ and jump condition* (1b) *across the interface Γ, then the following holds:*

(43) $$\mathcal{E}_h(t) \leq \mathcal{E}_h(0) \text{ for all } t \geq 0,$$

where $\mathcal{E}_h$ is obtained from $\mathcal{E}$ by replacing $\mathbf{U}$ by $\mathbf{U}_h$.

Proof. The IDG formulation consists of finding $\mathbf{U}_h$ satisfying

$$\sum_{T \in \mathcal{T}_h} \int_T \mathbf{V}_h^t \mathbf{S} \frac{\partial \mathbf{U}_h}{\partial t} dx dy + \mathcal{A}^c(\mathbf{V}_h, \mathbf{U}_h) + \mathcal{A}^u(\mathbf{V}_h, \mathbf{U}_h) = 0 \ \ \forall \, \mathbf{V}_h.$$

Testing against $\mathbf{U}_h$ we have

$$\frac{1}{2} \frac{d}{dt} \sum_{T \in \mathcal{T}_h} \int_T \mathbf{U}_h^t \mathbf{S} \mathbf{U}_h dx dy + \mathcal{A}^c(\mathbf{U}_h, \mathbf{U}_h) + \mathcal{A}^u(\mathbf{U}_h, \mathbf{U}_h) = 0.$$

By Lemma 4.2, $\mathcal{A}_T^c(\mathbf{U}_h, \mathbf{U}_h) = 0$ and thus we can write

$$\frac{d}{dt} \mathcal{E}_h(t) = -\mathcal{A}^u(\mathbf{U}_h, \mathbf{U}_h).$$

We further note that, if $\mathcal{Z}_h^0$ denotes the set of all interior edges in the mesh, we have

$$
\begin{aligned}
\mathcal{A}^u(\mathbf{U}_h, \mathbf{U}_h) &= -\frac{1-\beta}{2} \sum_{T \in \mathcal{T}_h} \int_{\partial T \setminus \partial \Omega} \mathbf{U}_h^{+\,t} \mathbf{S} |\mathbf{D}(\boldsymbol{\nu})| (\mathbf{U}_h^- - \mathbf{U}_h^+) ds \\
&= \frac{1-\beta}{2} \sum_{e \in \mathcal{Z}_h^0} \int_e (\mathbf{U}_h^- - \mathbf{U}_h^+)^t \mathbf{S} |\mathbf{D}(\boldsymbol{\nu})| (\mathbf{U}_h^- - \mathbf{U}_h^+) ds \geq 0,
\end{aligned}
$$

which yields

$$
\frac{d}{dt} \mathcal{E}_h(t) = -\frac{1-\beta}{2} \sum_{e \in \mathcal{Z}_h^0} \int_e [\mathbf{U}_h]^t \mathbf{S} |\mathbf{D}(\boldsymbol{\nu})| [\mathbf{U}_h] ds.
$$

A direct computation shows that for all unit vectors $\boldsymbol{\nu} = (n_x, n_x)^t$

$$
\mathbf{S}|\mathbf{D}(\boldsymbol{\nu})| = \begin{pmatrix} \frac{1}{c_i \rho_i} & 0 & 0 \\ 0 & c_i \rho_i n_x^2 & c_i \rho_i n_x n_y \\ 0 & c_i \rho_i n_x n_y & c_i \rho_i n_y^2 \end{pmatrix} \quad on \ \Omega_i \quad i = 1, 2,
$$

is a positive semidefinite matrix with eigenvalues $\lambda_1 = c_i \rho_i$, $\lambda_2 = \frac{1}{c_i \rho_i}$, $\lambda_3 = 0$. Integrating on $[0, t]$ we establish that $\mathcal{E}_h(t) = \mathcal{E}_h(0)$ if $\beta = 1$ and $\mathcal{E}_h(t) \leq \mathcal{E}_h(0)$ for $0 \leq \beta < 1$. $\qquad \square$

In order to solve acoustic problems using biquadratic IFE spaces with curved interfaces one has to compute integrals on elements with curved sides. Therefore, numerical integration must be used [30] yielding an IDG-NI formulation, where the resulting integration errors may induce numerical instabilities. Here we reduce their effects by using high-precision quadratures on all interface elements with curved interface. In the simulations we used a quadrature with a 19th degree of precision. Alternatively, a well-known skew-symmetric formulation [12] guaranteeing stability with respect to both exact and numerical integration may be used. On an arbitrary element T the skew DG formulation is given by

$$
\begin{aligned}
&\int_T \mathbf{V}_h^t \mathbf{S} \frac{\partial \mathbf{U}_h}{\partial t} dx dy + \frac{1}{2} \int_T \left(\mathbf{V}_h^t L(\mathbf{U}_h) - \mathbf{U}_h^t L(\mathbf{V}_h) \right) dx dy \\
&\quad + \frac{1}{2} \int_{\partial T} \mathbf{V}_h^t \mathbf{S} \left(2 \ \widehat{\mathbf{D}(\mathbf{n})\mathbf{U}}_h \ - \mathbf{D}(\mathbf{n})\mathbf{U}_h \right) ds = 0,
\end{aligned}
\tag{44}
$$

where the numerical flux $\widehat{\mathbf{D}(\mathbf{n})\mathbf{U}}_h$ is defined by (27).

Summing over all elements leads to a stable formulation without requiring interface terms. Theorem 4.3 holds for the skew IDG energy for all contrasts with exact and numerical integration.

In the next section we also perform a numerical study to display the stability properties of our IDG method described above and the immersed standard DG method obtained by testing against IFE functions $\mathbf{V} \in \mathcal{U}_h^{1,cf}(T)$ and using the numerical flux (27). More specifically, the spatial discretization leads to semidiscrete problems of the form

$$
\frac{d\mathbf{C}(t)}{dt} = \mathbf{K}\mathbf{C},
\tag{45}
$$

where $\mathbf{C} \in \mathbb{R}^N$ and $\mathbf{K} \in \mathbb{R}^{N \times N}$. In section 5 we will compute and plot the spectrum of $\mathbf{K}$ for each immersed method and discuss and compare their stability properties. For a more complete numerical study we refer the reader to [30].

During computations we observed that when an interface element of type I is cut by the interface such that the two interface points E or D are very close to a vertex A_i the time marching scheme requires small time steps. We addressed this issue by applying the classical fourth order Runge–Kutta (RK4) method with local time stepping which is desired for these interface problems where in each region we chose a time step according to its own CFL condition. For the purpose of saving space we refer the reader to [30] for a detailed description of a local time-stepping RK4 algorithm. In the future we will also investigate cell-agglomeration techniques used with X-FEM [25, 31] that merge small-cut elements with neighboring elements. This has been shown to improve the conditioning of the problem when arbitrarily small-cut elements are present in the mesh.

To speed up our IDG computations we implemented a parallel version of this algorithm using MPI on a cluster of processors. The reader may consult [30] for more details. The proposed parallel local time stepping IDG algorithm yields higher efficiency for interface problems with $c_1/c_2 >> 1$ or $c_1/c_2 << 1$.

5. Computational examples. We will conduct several numerical tests to show the approximation capabilities of the IFE spaces and the accuracy of the IDG method for acoustic problems with linear and curved interfaces. The first set of computations are conducted to discover the approximation capability of the proposed IFE spaces as well as the accuracy and order of convergence of the IDG solutions on a problem with two media separated by a linear interface. We conduct similar experiments on a second interface problem involving a circular interface. In our computations we used RK4 to integrate in time with global and local time stepping [30] with time steps that guarantee both the stability of the scheme (as dictated by CFL conditions and the presence of small-cut elements) and negligible temporal discretization errors compared to spatial errors. The small time steps used in some examples are due to the fact that we used the same time step for all meshes some of which contain small-cut elements. We used the true solution whenever needed at the boundary of the domain.

Example 5.1. First, we solve the two dimensional acoustic interface problem (2) with a linear interface subjected to an initial condition at $\mathbf{X} = (x, y)^t$ having the form

$$(46) \qquad \mathbf{U}_0(x, y) = \mathcal{A}_i \psi(\mathbf{k}_i \cdot \mathbf{X} - \omega_c t_0) \mathbf{Z}_i, \qquad \psi(\xi) = \sin(\xi) e^{-4\xi^2},$$

where $\mathbf{Z}_i = [1, \frac{\alpha_1}{\rho_1 c_1}, \frac{\alpha_2}{\rho_1 c_1}]^t$ and $\mathbf{k}_i = \frac{\omega_c}{c_1}(\alpha_1, \alpha_2)^t$ with $\alpha_1^2 + \alpha_2^2 = 1$. Finally, w_c is the wave frequency and $\mathcal{A}_i = 1$ is the amplitude of the incident wave. The incident wave starts in Ω_1 and moves with speed c_1 in the direction of the vector $(\alpha_1, \alpha_2)^t$ until it hits the linear interface to generate a reflected and a transmitted wave. To be more specific we consider the domain $\Omega = (0, 20)^2$ divided by the linear interface $\Gamma = \{(x, y) \mid y = -6.6667x + 86.408\}$ into $\Omega_1 = \{(x, y) \in \Omega \mid y < -6.6667x + 86.408\}$ and $\Omega_2 = \{(x, y) \in \Omega \mid y > -6.6667x + 86.408\}$. For this test problem we assume that for the medium occupying Ω_1, $c_1 = 1 m/s$, $\rho_1 = 1 kg/m^3$ and for the medium occupying Ω_2, $c_2 = 2 m/s$, $\rho_2 = 1.5 kg/m^3$. For the initial condition (46) we select $t_0 = 12.4911$, $\omega_c = 1$, $(\alpha_1, \alpha_2) = (2, 1)/\sqrt{5}$, and the inflow boundary condition on $\partial\Omega$ is computed using the true solution computed following [23, 24].

TABLE 1
L^2 errors and orders of convergence with $\mathcal{U}_h^{1,cf}$ spaces at $t = 5$ for Example 5.1.

N	$\frac{\|p-p_h\|_{L^2}}{\|p\|_{L^2}}$	Order	$\frac{\|u-u_h\|_{L^2}}{\|u\|_{L^2}}$	Order	$\frac{\|v-v_h\|_{L^2}}{\|v\|_{L^2}}$	Order
100^2	9.9832e-3	NA	1.8502e-2	NA	1.3050e-2	NA
150^2	4.4706e-3	1.9814	8.2891e-3	1.9803	5.8534e-3	1.9774
200^2	2.5205e-3	1.9920	4.6750e-3	1.9908	3.3050e-3	1.9869
250^2	1.6148e-3	1.9953	2.9956e-3	1.9946	2.1193e-3	1.9913
300^2	1.1220e-3	1.9969	2.0816e-3	1.9965	1.4735e-3	1.9936
350^2	8.2463e-4	1.9978	1.5300e-3	1.9975	1.0834e-3	1.9950
400^2	6.3150e-4	1.9984	1.1717e-3	1.9981	8.2992e-4	1.9959

TABLE 2
L^2 errors and orders of convergence for $\mathcal{U}_h^{2,cf}$ spaces at $t = 5$ for Example 5.1.

N	$\frac{\|p-p_h\|_{L^2}}{\|p\|_{L^2}}$	Order	$\frac{\|u-u_h\|_{L^2}}{\|u\|_{L^2}}$	Order	$\frac{\|v-v_h\|_{L^2}}{\|v\|_{L^2}}$	Order
100^2	7.7237e-4	NA	1.4925e-3	NA	1.0278e-3	NA
150^2	2.3092e-4	2.9778	4.4960e-4	2.9591	3.0650e-4	2.9841
200^2	9.7745e-5	2.9884	1.9097e-4	2.9764	1.2978e-4	2.9873
250^2	5.0114e-5	2.9939	9.8207e-5	2.9804	6.6549e-5	2.9931
300^2	2.9025e-5	2.9954	5.6924e-5	2.9911	3.8542e-5	2.9957
350^2	1.8286e-5	2.9971	3.5917e-5	2.9874	2.4286e-5	2.9961
400^2	1.2254e-5	2.9978	2.4089e-5	2.9916	1.6275e-5	2.9975

In order to show the approximation capability of the spaces $\mathcal{U}_h^{k,cf}$ we compute the L^2 projection of the true solution onto $\mathcal{U}_h^{k,cf}$ on uniform Cartesian meshes having $N = n^2$, $n = 50l$, $l = 2, 3, \ldots, 8$, and present the L^2 errors and orders of convergence in Tables 1 and 2 which suggest optimal convergence rates.

Now we solve the problem on the same meshes with $\mathcal{U}_h^{k,cf}$, $k = 1, 2$. We integrate in time from $t = 0$ to $t = 5$ using a local time-stepping RK4 scheme with $\Delta t_1 = 2 \cdot 10^{-3}$ on all noninterface elements in Ω_1 and $\Delta t_2 = 10^{-3}$ on the remaining elements using bilinear IFE spaces. Similarly, we used $\Delta t_1 = 10^{-3}$ on noninterface elements in Ω_1 and $\Delta t_2 = 5 \cdot 10^{-4}$ on the remaining elements for the biquadratic IFE spaces. These time steps guarantee the stability of the scheme and yield negligible temporal discretization errors compared to spatial errors. We present the L^2 errors for the pressure and velocity and their orders of convergence at $t = 5$ in Tables 3 and 4 which suggest optimal convergence rates. The IDG solutions and pointwise errors on a uniform mesh having $N = 200^2$ square elements with bilinear IFE spaces are shown in Figure 6. IDG solutions and errors for the spaces $\mathcal{U}_h^k$ are similar and are not shown here.

In order to compare the approximation capabilities of our IFE spaces $\mathcal{U}_h^{k,cf}$ and $\mathcal{U}_h^k$, we solve the previous problem with the same parameters as above using $\mathcal{U}_h^k$, $k = 1, 2$. We plot $\|\nabla \times \mathbf{v}_h\|_{L^2}$ and the L^2 IDG errors for both velocity and pressure versus mesh size in Figure 7. We observe that the results are indistinguishable for both IFE spaces and exhibit optimal convergence rates. However, the smaller IFE spaces satisfying the curl-free interface conditions are more efficient.

Example 5.2. In the second test problem we consider the acoustic interface problem (2) on the domain $\Omega = (0, 20)^2$ divided by the circle $\Gamma = \{(x, y) \mid (x - x_0)^2 + $

TABLE 3

L^2 IDG errors and orders of convergence at $t = 5$ for Example 5.1 using $\mathcal{U}_h^{1,cf}$.

N	$\frac{\|p-p_h\|_{L_2}}{\|p\|_{L_2}}$	Order	$\frac{\|u-u_h\|_{L_2}}{\|u\|_{L_2}}$	Order	$\frac{\|v-v_h\|_{L_2}}{\|v\|_{L_2}}$	Order
100^2	9.0588e-2	NA	1.2189e-1	NA	1.0245e-1	NA
150^2	3.2884e-2	2.4992	4.5591e-2	2.4254	3.7864e-2	2.4548
200^2	1.5020e-2	2.7239	2.1260e-2	2.6518	1.7590e-2	2.6649
250^2	8.0408e-3	2.8002	1.1607e-2	2.7124	9.6011e-3	2.7134
300^2	4.8098e-3	2.8185	7.0838e-3	2.7082	5.8708e-3	2.6979
350^2	3.1189e-3	2.8102	4.6889e-3	2.6767	3.8982e-3	2.6564
400^2	2.1493e-3	2.7884	3.2987e-3	2.6336	2.7532e-3	2.6042

TABLE 4

L^2 IDG errors and orders of convergence at $t = 5$ for Example 5.1 using $\mathcal{U}_h^{2,cf}$.

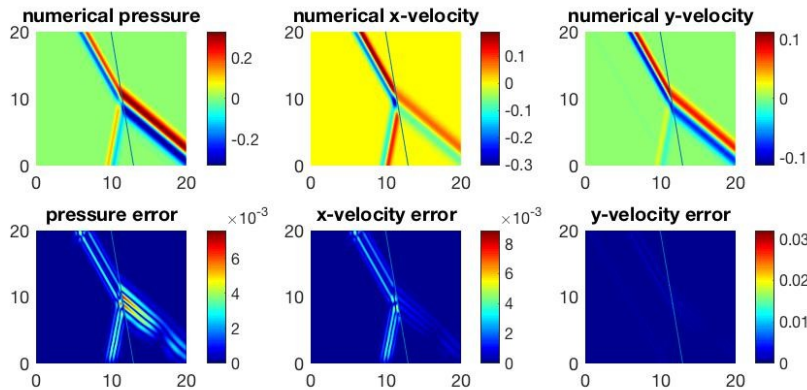| N	$\frac{\|p-p_h\|_{L_2}}{\|p\|_{L_2}}$	Order	$\frac{\|u-u_h\|_{L_2}}{\|u\|_{L_2}}$	Order	$\frac{\|v-v_h\|_{L_2}}{\|v\|_{L_2}}$	Order
100^2	2.0712e-3	NA	3.4645e-3	NA	2.6283e-3	NA
150^2	4.1962e-4	3.9376	8.2574e-4	3.5368	6.2646e-4	3.5367
200^2	1.5618e-4	3.4356	3.2863e-4	3.2026	2.5607e-4	3.1098
250^2	7.6806e-5	3.1805	1.6700e-4	3.0336	1.3286e-4	2.9405
300^2	4.3782e-5	3.0828	9.6443e-5	3.0115	7.8913e-5	2.8574
350^2	2.7395e-5	3.0416	6.0840e-5	2.9886	5.0554e-5	2.8887
400^2	1.8312e-5	3.0166	4.0940e-5	2.9668	3.4556e-5	2.8493

FIG. 6. IDG solution (top) and errors (bottom) at $t = 5$ for Example 5.1 with $N = 200^2$ elements and using $\mathcal{U}_h^{1,cf}$.

$(y - y_0)^2 = a^2\}$ into the exterior $\Omega_1 = \{(x, y) \in \Omega \mid (x - x_0)^2 + (y - y_0)^2 > a^2\}$ and the interior $\Omega_2 = \{(x, y) \in \Omega \mid (x - x_0)^2 + (y - y_0)^2 < a^2\}$.

In order to compute the errors and rate of convergence for the IDG method we again need the true pressure which is computed [11] using truncated infinite series. For all remaining examples we apply periodic boundary conditions.

To show the approximation capabilities of IFE spaces and convergence rates for the IDG method, we solve the acoustic problem subject to initial condition (46) with $t_0 = 4$, $w_c = 1$, and $(\alpha_1, \alpha_2) = (1, 0)$ on the domain $(0, 20)^2$ with the circular interface
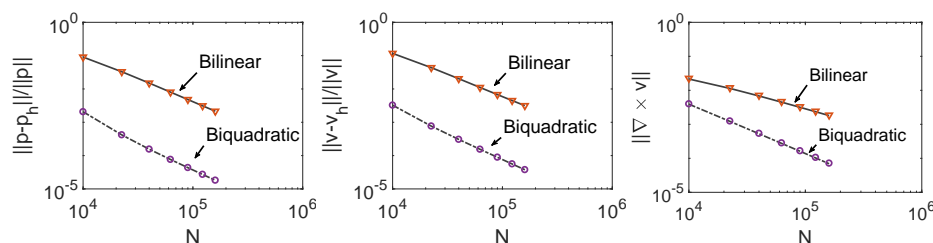
FIG. 7. L^2 IDG errors in pressure (left) and velocity (center) and L^2 norm $||\nabla \times \mathbf{v}||$ (right) for $\mathcal{U}_h^{1,cf}$ (solid) and $\mathcal{U}_h^{2,cf}$ (discontinuous). Errors are marked by ($\triangledown$) using $\mathcal{U}_h^1$ and by (o) using $\mathcal{U}_h^2$ for Example 5.1.

TABLE 5

L^2 IDG errors and orders of convergence at $t = 3$ for Example 5.2 using $\mathcal{U}_h^{k,cf}$, $k = 1, 2$.

	Bilinear		Biquadratic	
N	$\| p - p_h \|_{L_2}$	Order	$\| p - p_h \|_{L_2}$	Order
100^2	1.2711e-1	NA	3.9953e-3	NA
150^2	4.6997e-2	2.4539	8.8820e-4	3.7085
200^2	2.1814e-2	2.6680	3.4437e-4	3.2934
250^2	1.1867e-2	2.7282	1.7160e-4	3.1216
300^2	7.2184e-3	2.7266	9.8278e-5	3.0571
350^2	4.7649e-3	2.6944	6.1626e-5	3.0276
400^2	3.3421e-3	2.6562	4.1200e-5	3.0154

centered at $(x_0, y_0) = (10.02531, 10.04241)$ and radius $a = 4$. For convenience, we chose special values for center coordinates in order to avoid interface elements that are cut very close to the corners which require small times steps as discussed in section 4. Here the speeds and densities are the same as in Example 5.1. A planar wave starts in Ω_1 and moves with speed c_1 in the direction of the vector $(1, 0)^t$ until it hits the circular interface. We use $\mathcal{U}_h^{1,cf}$ and integrate in time from $t = 0$ to $t = 3$ using RK4 with the local time steps $\Delta t_1 = 2 \cdot 10^{-4}$ on all noninterface elements in Ω_1 and $\Delta t_2 = 10^{-4}$ on the remaining elements. For $\mathcal{U}_h^{2,cf}$ we use RK4 with local time steps $\Delta t_1 = 10^{-4}$ on all noninterface elements in Ω_1 and $\Delta t_2 = 5 \cdot 10^{-5}$ on the remaining elements. We present in Table 5 the true L^2 errors and their orders of convergence on uniform square meshes having $N = n^2$ squares, with $n = 50l$, $l = 2, 3, \ldots, 8$, for bilinear and biquadractic IFE spaces. The results of Table 5 show that IFE spaces are optimal. Finally, we plot in Figure 8 the numerical pressures and pointwise errors at $t = 3$ on a 200^2-element uniform mesh with $\mathcal{U}_h^{1,cf}$. Again, results for $\mathcal{U}_h^1$ and $\mathcal{U}_h^2$ are similar and are not shown.

Example 5.3. In order to show the performance of the IDG method on a high contrast problem we consider the interface acoustic problem (2) on the domain $\Omega = [0, 200]^2$ with a circular interface centered at $(x_0, y_0) = (115.01111, 110.01111)$ with radius $a = 40$, where Ω_1 (outside circle) is occupied by water with $c_1 = 1500$ m/s, $\rho_1 = 1000$ kg/m^3, and Ω_2 (inside circle) is occupied by air with $c_2 = 340$ m/s and $\rho_2 = 1.3$ kg/m^3. The initial condition is given by (46) with $t_0 = 0.04$, $\omega_c = 100$, and $(\alpha_1, \alpha_2) = (1, 0)$ and apply periodic boundary conditions. A planar initial wave starts in Ω_1 and propagates with speed c_1 in the direction of $(1, 0)^t$ until it hits the circular
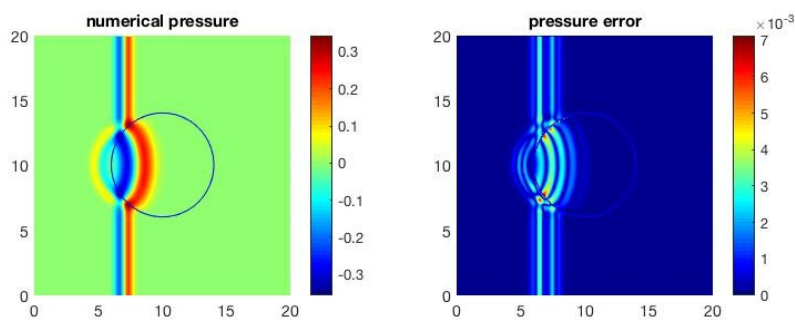
FIG. 8. *IDG pressures (left) and errors (right) at* $t = 3$ *for Example* 5.2 *using* $\mathcal{U}_h^{1,cf}$ *and* $N = 200^2$ *elements.*
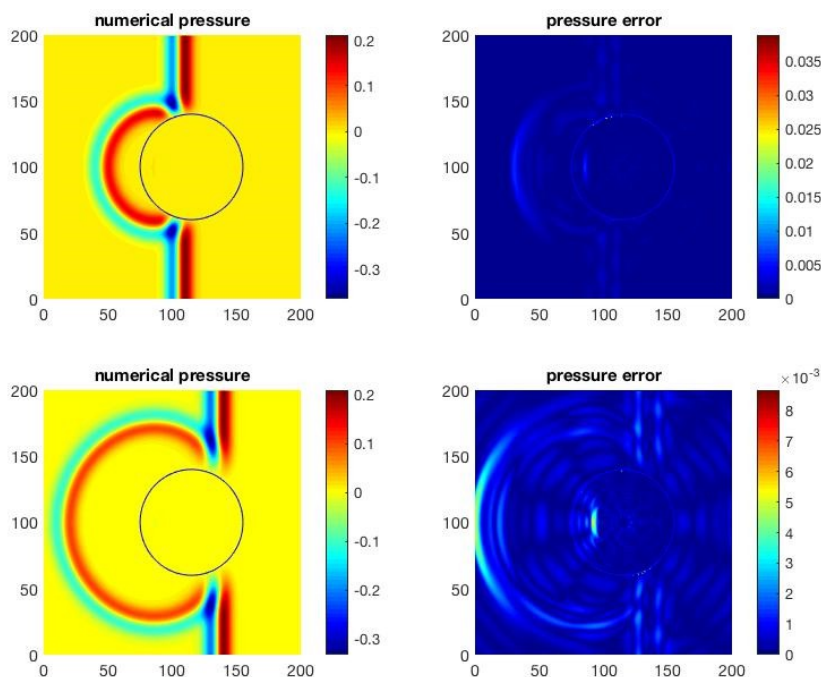

FIG. 9. *IDG pressures (left) and errors (right) for Example* 5.3 *at* $t = 0.03, 0.05$ *(top to bottom) using* $\mathcal{U}_h^{1,cf}$.

interface. We apply the IDG method described in section 4 combined with RK4 to integrate in time from $t = 0$ to $t = 0.05$ with the global time step $\Delta t = 10^{-7}$. This problem simulates an air bubble immersed in water where the incident acoustic wave is reflected and a small amplitude wave is transmitted. We plot the IDG solutions and corresponding pointwise errors in Figure 9.

Example 5.4. Here we perform a numerical study of the stability of immersed methods with both standard DG and our IDG formulation. We consider the previous water/air interface problem on $\Omega = [0, 40]^2$ with a circular interface of radius 10 and center $(x_0, y_0) = (20.1111, 20.1111)$ on a 10×10 Cartesian mesh using $\mathcal{U}_h^{1,cf}$. We show the spectra of the matrix **K** given by (45) in Figure 10. The immersed standard DG

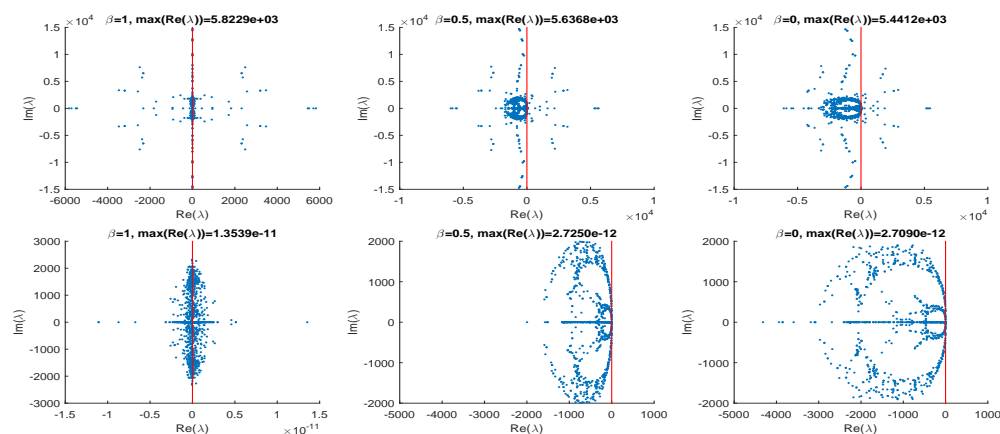FIG. 10. *Eigenvalues of* **K** *for standard DG (top) and IDG (bottom) with* $\beta = 1$ *(left),* $\beta = 0.5$ *(center),* $\beta = 0$ *(right) using* $\mathcal{U}_h^{1,cf}$ *for water/air problem.*

TABLE 6
Spectral radii of **K** *versus contrast on a fixed mesh and fixed interface (left) and versus* ϵ/h *on a fixed mesh for water/air problem (right).*

c_1	ρ_1	c_2	ρ_2	$\rho(\mathbf{K})$
1500	1000	340	1.3	4.3185e+3
1500	1000	340	13	4.3321e+3
1500	1000	340	130	4.3522e+3
1500	1000	34	1.3	4.3150e+3
1500	1000	1000	1.3	4.3460e+3
1500	1000	500	1.3	4.3226e+3
1500	1000	100	1.3	4.3154e+3
1500	1000	50	1.3	4.3150e+3

ϵ/h	$\rho(\mathbf{K})$
0.1	4.3313e+3
0.01	1.1288e+4
0.001	1.0577e+5
0.0001	1.0574e+6

method is unstable as several eigenvalues of **K** are in the right half-plane. However, the eigenvalues of **K** for the IDG method with central flux are on the imaginary axis while those for upwinding fluxes are in the left half-plane in full agreement with theory. See [30] for more numerical results. Spectra for the water/hydrogen interface problem are similar and are omitted.

Next, we conduct two experiments and show the resulting spectral radii $\rho(\mathbf{K})$ of **K** in Table 6. First, we compute $\rho(\mathbf{K})$ corresponding to the IDG method applied to the above acoustic problem with varying contrasts on a fixed mesh and fixed interface. In the second experiment we fix the mesh and contrast (water/air) and move the center of the circular interface $(20 + \delta, 20)$, where δ is such that $\epsilon/h = 0.1, 0.01, 0.001, 0.0001$ and compute corresponding spectral radii. See Figure 11 for an illustration of the mesh used and a small-cut element with the notation ϵ.

The spectral radii in Table 6 suggest that $\rho(\mathbf{K})$ is independent of the contrast on a fixed mesh and fixed interface. However, $\rho(\mathbf{K})$ gets larger in the presence of small-cut elements as $\epsilon/h \to 0$.

6. Conclusion. A second and a third order weighted IDG finite element method is developed for two dimensional acoustic wave propagation in inhomogeneous media. On noninterface elements we use standard polynomial spaces while on an interface element containing two fluids we construct special piecewise polynomial IFE spaces
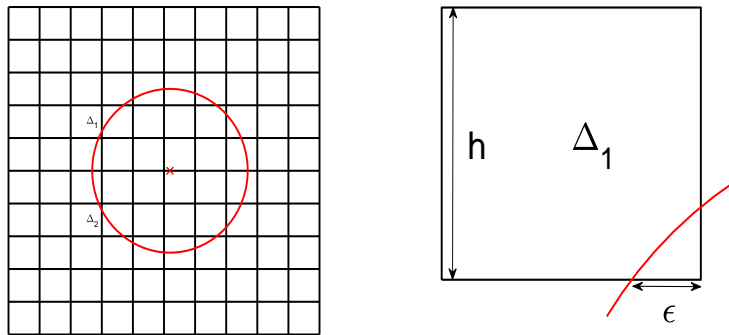
FIG. 11. *An illustration of a mesh and small-cut element.*

satisfying interface jump conditions. The new IFE spaces are optimal and are combined with a weighted weak DG formulation leading to efficient second and third order finite element methods for acoustic wave propagation in inhomogeneous media. The proposed methods are stable for all contrasts on a fixed mesh and fixed interface.

In the future we plan to establish a priori error estimates for the IFE approximation errors and the accuracy of the proposed IDG method in order to determine whether the constants involved depend on the contrast. Furthermore, we will investigate the dependence of the CFL number on the contrast and address the issue of small-cut elements by using cell-agglomeration techniques. We also plan to extend this work to other wave propagation interface problems.

Acknowledgments. The authors would like to thank David Kopriva and Tim Warburton for their helpful suggestions.

REFERENCES

[1] S. ADJERID, M. BEN-ROMDHANE, AND T. LIN, *Higher degree immersed finite element methods for second-order elliptic interface problems*, Int. J. Numer. Anal. Model., 11 (2014), pp. 541–556.

[2] S. ADJERID, M. BEN-ROMDHANE, AND T. LIN, *Quadratic immersed finite element spaces for elliptic interface problems*, in Advances in Applied Mathematics, Springer Proc. Math. Stat. 18, A. Ansari and H. Temimi, eds., Springer, New York, 2014, pp. 171–178, https://doi.org/10.1007/978-3-319-06923-4_16.

[3] S. ADJERID, M. BEN-ROMDHANE, AND T. LIN, *Higher degree immersed finite element spaces constructed according to the actual interface*, Comput. Math. Appl., 75 (2018), pp. 1868–1881.

[4] S. ADJERID, N. CHAABANE, AND T. LIN, *An immersed discontinuous finite element method for Stokes interface problems*, Comput. Methods Appl. Mech. Engrg., 293 (2015), pp. 170–190, https://doi.org/10.1016/j.cma.2015.04.006.

[5] S. ADJERID AND T. LIN, *Higher-order immersed discontinuous Galerkin methods*, Int. J. Inf. Syst. Sci., 3 (2007), pp. 558–565.

[6] S. ADJERID AND T. LIN, *p-th degree immersed finite element for boundary value problems with discontinuous coefficients*, Appl. Numer. Math., 59 (2009), pp. 1303–1321.

[7] S. ADJERID AND K. MOON, *A higher order immersed discontinuous Galerkin finite element method for the acoustic interface problem*, in Advances in Applied Mathematics 18, A. Ansari and H. Temimi, eds., Springer, New York, 2014, pp. 57–69, https://doi.org/10.1007/978-3-319-06923-4_6.

[8] I. BABUSKA AND J. E. OSBORN, *Generalized finite element methods: Their performance and their relation to mixed methods*, SIAM J. Numer. Anal., 20 (1983), pp. 510–536.

[9] J. W. Banks, W. D. Henshaw, and D. W. Schwendeman, *Deforming composite grids for solving fluid structure problems*, J. Comput. Phys., 231 (2012), pp. 3518–3547.

[10] T. Belytschko, N. Moës, S. Usui, and C. Primi, *Arbitrary discontinuities in finite elements*, Internat. J. Numer. Methods Engrg., 50 (2001), pp. 993–1013.

[11] J. Bowman, T. B. A. Senior, and P. L. E. Uslenghi, *Electromagnetic and Acoustic Scattering by Simple Shapes*, 1st ed., CRC Press, Boca Raton, FL, 1988.

[12] C. Canuto, M. Y. Hussaini, A. Quarteroni, and T. A. Zang, *Spectral Methods, Fundamentals in Single Domains*, Springer, New York, 2006.

[13] B. Cockburn, S. Lin, and C.-W. Shu, *TVB Runge-Kutta local projection discontinuous Galerkin methods of scalar conservation laws III: One dimensional systems*, J. Comput. Phys., 84 (1989), pp. 90–113.

[14] B. Cockburn and C.-W. Shu, *TVB Runge-Kutta local projection discontinuous Galerkin methods for scalar conservation laws II: General framework*, Math. Comp., 52 (1989), pp. 411–435, https://doi.org/10.2307/2008474.

[15] V. Dolesji and M. Feistauer, *Discontinuous Galerkin Method*, Springer, Cham, Switzerland, 2015.

[16] R. S. Falk and G. R. Richter, *Explicit finite element methods for symmetric hyperbolic equations*, SIAM J. Numer. Anal., 36 (1999), pp. 935–952.

[17] X. He, T. Lin, and Y. Lin, *Approximation capability of a bilinear immersed finite element space*, Numer. Methods Partial Differential Equations, 24 (2008), pp. 1265–1300.

[18] X. He, T. Lin, and Y. Lin, *Interior penalty bilinear IFE discontinuous Galerkin methods for elliptic equations with discontinuous coefficient*, J. Syst. Sci. Complex., 23 (2010), pp. 467–483.

[19] W. D. Henshaw, *A high-order accurate parallel solver for Maxwell's equations on overlapping grids*, SIAM J. Sci. Comput., 28 (2006), pp. 1730–1765.

[20] J. Hesthaven and T. Warburton, *Nodal high-order methods on unstructured grids-I. Time-domain solution of Maxwell's equations*, J. Comput. Phys., 181 (2002), pp. 186–221.

[21] J. S. Hesthaven and T. Warburton, *Nodal Discontinuous Galerkin Methods*, Texts Appl. Math. 54, Springer, New York, 2008.

[22] R. Kafafy, T. Lin, Y. Lin, and J. Wang, *Three-dimensional immersed finite element methods for electric field simulation in composite materials*, Internat. J. Numer. Methods Engrg., 64 (2005), pp. 904–972.

[23] D. A. Kopriva, *Implementing Spectral Methods for Partial Differential Equations*, Algorithms for Scientists and Engineers, Springer, Dordrecht, The Netherlands, 2009.

[24] D. A. Kopriva. Private communication, 2013.

[25] F. Kummer, *Extended discontinuous Galerkin methods for two-phase flows: The spatial discretization*, Internat. J. Numer. Methods Engrg., 109 (2017), pp. 259–289.

[26] Z. Li, *The immersed interface method using a finite element formulation*, Appl. Numer. Math., 27 (1998), pp. 253–267.

[27] Z. Li and K. Ito, *The Immersed Interface Method: Numerical Solutions of PDEs Involving Interfaces and Irregular Domains*, Front. Appl. Math. 33, SIAM, Philadelphia, 2006.

[28] T. Lin and X. Zhang, *Linear and bilinear immersed finite elements for planar elasticity interface problems*, J. Comput. Appl. Math., 236 (2012), pp. 4681–4699.

[29] B. Lombard and J. Piraux, *Numerical treatment of two dimensional interfaces for acoustic and elastic waves*, J. Comput. Phys., 195 (2004), pp. 90–116.

[30] K. Moon, *Immersed Discontinuous Galerkin Methods for Acoustic Wave Propagation in Inhomogeneous Media*, Ph.D. thesis, Virginia Tech, Blacksburg, VA, 2016.

[31] B. Muller, S. Kramer-Eis, F. Kummer, and M. Oberlack, *A high-order discontinuous Galerkin method for compressible flows with immersed boundaries*, Internat. J. Numer. Methods Engrg., 110 (2017), pp. 3–30.

[32] D. A. D. Pietro and A. Ern, *Mathematical Aspects of Discontinuous Galerkin Methods*, Math. Appl. (Berlin) 69, Springer, Heidelberg, 2012.

[33] W. Reed and T. Hill, *Triangular mesh methods for the neutron transport equation*, Technical report LA-UR-73-479, Los Alamos Scientific Laboratory, Los Alamos, NM 1973.

[34] B. Rivière, *Discontinuous Galerkin Methods for Solving Elliptic and Parabolic Equations*, Front. Appl. Math., F35, SIAM, Philadelphia, 2008.